

Electronic Structure of Tetrahedral, $S = 2$, $[\text{Fe}\{(\text{E}^i\text{Pr}_2)_2\text{N}\}_2]$, $E = \text{S}, \text{Se}$, Complexes: Investigation by High-Frequency and -Field Electron Paramagnetic Resonance, ^{57}Fe Mössbauer Spectroscopy, and Quantum Chemical Studies

Sebastian A. Stoian,* Mahsa Moshari, Eleftherios Ferentinos, Alexios Grigoropoulos, J. Krzystek, Joshua Telser, and Panayotis Kyritsis*

Cite This: *Inorg. Chem.* 2021, 60, 10990–11005

Read Online

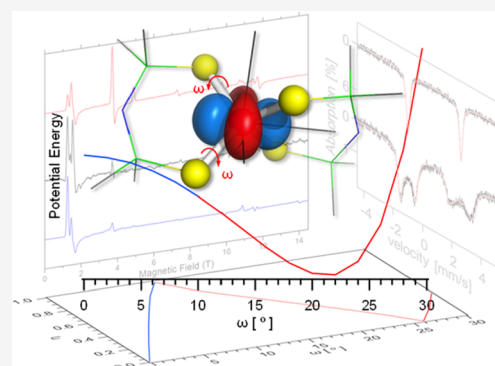
ACCESS |

Metrics & More

Article Recommendations

Supporting Information

ABSTRACT: In this work, we assessed the electronic structures of two pseudotetrahedral complexes of Fe^{II} , $[\text{Fe}\{(\text{S}^i\text{Pr}_2)_2\text{N}\}_2]$ (**1**) and $[\text{Fe}\{(\text{Se}^i\text{Pr}_2)_2\text{N}\}_2]$ (**2**), using high-frequency and -field EPR (HF-EPR) and field-dependent ^{57}Fe Mössbauer spectroscopies. This investigation revealed $S = 2$ ground states characterized by moderate, negative zero-field splitting (zfs) parameters D . The crystal-field (CF) theory analysis of the spin Hamiltonian (sH) and hyperfine structure parameters revealed that the orbital ground states of **1** and **2** have a predominant $d_{x^2-y^2}$ character, which is admixed with d_z^2 ($\sim 10\%$). Although replacing the S-containing ligands of **1** by their Se-containing analogues in **2** leads to a smaller $|D|$ value, our theoretical analysis, which relied on extensive *ab initio* CASSCF calculations, suggests that the ligand spin–orbit coupling (SOC) plays a marginal role in determining the magnetic anisotropy of these compounds. Instead, the $d_{x^2-y^2}^{\beta} \rightarrow d_{xy}^{\beta}$ excitations yield a large negative contribution, which dominates the zfs of both **1** and **2**, while the different energies of the $d_{x^2-y^2}^{\beta} \rightarrow d_{xz}^{\beta}$ transitions are the predominant factor responsible for the difference in zfs between **1** and **2**. The electronic structures of these compounds are contrasted with those of other $[\text{FeS}_4]$ sites, including reduced rubredoxin by considering a D_2 -type distortion of the $[\text{Fe}(\text{E}-\text{X})_4]$ cores, where $E = \text{S}, \text{Se}$; $X = \text{C}, \text{P}$. Our combined CASSCF/DFT calculations indicate that while the character of the orbital ground state and the quintet excited states' contribution to the zfs of **1** and **2** are modulated by the magnitude of the D_2 distortion, this structural change does not impact the contribution of the excited triplet states.



1. INTRODUCTION

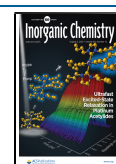
A common feature in biological inorganic chemistry is the presence of sulfur-containing ligands in the active site of metalloproteins, most usually in the form of cysteine thiolate (SCys) or inorganic sulfide, S^{2-} .^{1,2} The most prominent manifestation of biological metal–sulfur bonding is the active site of iron–sulfur proteins, which exhibit an impressive variety of structural and functional features.³ The simplest iron–sulfur protein is the electron transfer protein rubredoxin, (Rd), which contains a tetrahedral $[\text{Fe}^{\text{II/III}}(\text{SCys})_4]^{2-/1-}$ active site.⁴ Equivalent sites are also found in the non-heme iron protein desulfurodoxin^{5,6} and, as a secondary site, in Class I superoxide reductases (SORs).⁵ To elucidate their electronic structure and the factors that impact their biological function, significant research efforts have been made to synthesize analogues of reduced rubredoxins (Rd_{red}). The majority of these species are Fe^{II} complexes containing aryl- or phenyl-thiolates as ligands,^{7–12} but compounds containing monodentate alkyl-thiols¹³ and bidentate dithiosquarate⁸ or S_2 -*o*-xyl^{14,15} (where S_2 -*o*-xyl \equiv *o*-xyl- α, α' -methyl dithiolate) ligands have also

been structurally and spectroscopically characterized and are listed in Table 1. A detailed overview of the electronic properties of these compounds is presented in the Supporting Information (SI), section S1.

Another ligand platform with four S– or Se– (and even Te–) donors that has been employed to generate pseudo-tetrahedral complexes is the bidentate dichalcogenidoimidodiphosphinato ligand, $\{(\text{EPR}_2)_2\text{N}\}^-$ ($E = \text{S}, \text{Se}, \text{Te}$; $R = \text{alkyl}$ or aryl group bonded to the P atoms of the ligand). The overview included in the SI, section S1, also discusses the effect of selenium versus sulfur coordination in Fe^{II} and other 3d metal ion complexes. Of direct relevance here are compounds containing the $\text{Fe}^{\text{II}}\text{Se}_4$ core that have been structurally

Received: March 5, 2021

Published: July 21, 2021



characterized,^{16–23} but have not been studied as yet by either EPR or Mössbauer spectroscopy, with the exception of $[\text{Fe}\{(\text{SePPh}_2)_2\text{N}\}_2]$.²³ Two Fe^{II} complexes, $[\text{Fe}\{(\text{SPMe}_2)_2\text{N}\}_2]$ and $[\text{Fe}\{(\text{SPPH}_2)_2\text{N}\}_2]$,^{24–26} were reported in 1971.^{27,28} X-ray crystallography showed that $[\text{Fe}\{(\text{SPMe}_2)_2\text{N}\}_2]$ exhibits a tetrahedral $\text{Fe}^{\text{II}}\text{S}_4$ first coordination sphere and, therefore, may be regarded as a structural analogue of Rd_{red} .²⁷ The spectroscopic investigation of $[\text{Fe}\{(\text{SPPH}_2)_2\text{N}\}_2]$ by UV–vis,²⁸ resonance Raman,^{29,30} and, more recently, multi-frequency EPR spectroscopies (275.7, 94.1, and 9.5 GHz)³¹ revealed EPR signals attributed to more than one distinct $S = 2$ Fe^{II} site evidencing the occurrence, in the same crystal, of similar but distinct structural conformations. The spin-Hamiltonian (sH) parameters, g values and axial D , and rhombic E zero-field splitting (zfs) parameters of $[\text{Fe}\{(\text{SPPH}_2)_2\text{N}\}_2]$ were accurately determined by the EPR studies, which revealed that this compound exhibits a moderate zfs, described by a positive D value.³¹

Recently, the $[\text{Fe}\{(\text{EP}^i\text{Pr}_2)_2\text{N}\}_2]$, $E = \text{S}$ (**1**) and Se (**2**) complexes, incorporating ^iPr as peripheral R groups, as opposed to $R = \text{Me}$ and Ph , were synthesized and structurally characterized.³² This study revealed that **1** and **2** exhibit tetrahedral $\text{Fe}^{\text{II}}\text{E}_4$ coordination spheres and that they are isomorphous, see Figure 1. The reported structures displayed

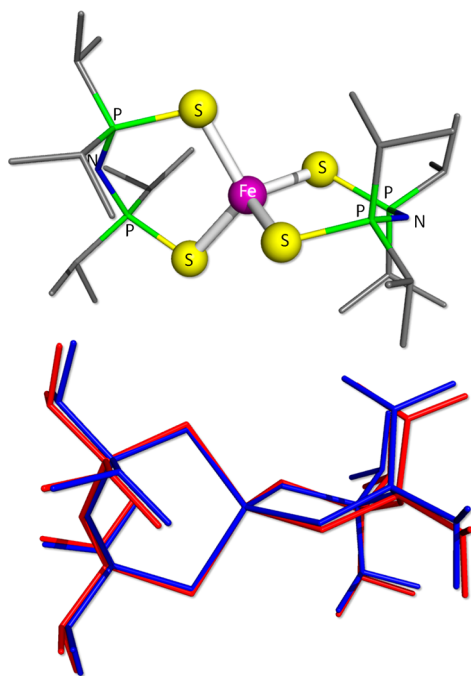


Figure 1. Top: crystal structure of the site a of **1**. Bottom: overlay of the structures of site a of **1** (blue) and **2** (red).

two distinct sites per unit cell, with conformations close to those expected for enantiomers, see Figure S1. Inspection of Figure S1 reveals that for these molecules, chirality may be traced to the second coordination sphere of the iron sites.

X- (~ 9 GHz) and Q-band (~ 35 GHz) EPR, usually employing parallel-mode detection, are often used to study high-spin ($S = 2$) Fe^{II} sites in proteins^{33–36} and metal complexes.³⁷ However, because the use of a single (and low) EPR frequency seldom provides more than one resonance out of multiple possible transitions, this method is of limited value for these and other integer spin systems. For this reason, over

the last few years, high-frequency and -field EPR (HFEP) has been employed extensively to investigate the electronic properties of a wide range of transition metal complexes^{38–40} and certain metalloproteins.^{41,42} Nevertheless, only a small number of tetrahedral $\text{Fe}^{\text{II}}\text{S}_4$ -containing systems have been studied by HFEP, namely, $[\text{Ph}_4\text{P}]_2[\text{Fe}(\text{SPh})_4]$,⁴³ Rd_{red} (see footnote e of Table 1),⁴⁴ and three compounds containing the $[\text{Fe}(\text{C}_3\text{S}_5)_2]^{2-}$ complex anion.⁴⁵ In addition, HFEP studies have been performed on a trigonal pyramidal complex exhibiting an $\text{Fe}^{\text{II}}\text{N}_4$ first coordination sphere,⁴⁶ as well as on six-coordinated Fe^{II} complexes.³⁹ Mössbauer spectroscopy has also been employed to elucidate the electronic structure of the $\text{Fe}^{\text{II}}\text{S}_4$ -core in biomimetic inorganic complexes^{8,47,48} and rubredoxin.^{49–53} Recently, the investigation by magnetometry, HFEP (at 275.7 GHz), and Mössbauer spectroscopy of the $[\text{Fe}\{(\text{SePPh}_2)_2\text{N}\}_2]$ complex, exhibiting a tetrahedral $\text{Fe}^{\text{II}}\text{Se}_4$ first coordination sphere, was reported.²³

Herein, the electronic structure of **1** and **2** was probed by HFEP and field-dependent Mössbauer spectroscopy. Based on these studies, it was possible to accurately determine not only the spin Hamiltonian (sH) parameters but also the electric field gradient (efg) and the hyperfine coupling tensor \mathbf{A} of the ^{57}Fe center. The electronic structures of these compounds were also explored using computational studies including *ab initio* quantum chemical calculations. Comparing **1** with **2** allowed us to elucidate the effect of the first (FeS_4 vs FeSe_4) coordination sphere on the electronic structure of these complexes. We also compared the electronic structures of **1** and **2** to those of other tetrahedral $\text{Fe}^{\text{II}}\text{E}_4$ -containing systems ($E = \text{S}, \text{Se}$). In this respect, the experimentally determined sH parameters of complex **2** are useful benchmarks, complementing recent computational studies on the $\text{M}^{\text{II}}\text{Se}_4$ -containing tetrahedral $[\text{M}\{(\text{SeP}^i\text{Pr}_2)_2\text{N}\}_2]$, $\text{M} = \text{Ni},^{54} \text{Co},^{55}$ complexes. Our combined experimental and computation investigations establish well-defined magnetostructural correlations for this class of tetrahedral Fe^{II} complexes. The complexes studied in this work are also of interest from the molecular magnetism point of view, since tetrahedral $S = 2$ Fe^{II} complexes have been recently found to exhibit slow relaxation of magnetization.^{45,56–58} The results of a detailed investigation of complexes **1** and **2** by alternate current magnetometry will be reported elsewhere.

2. MATERIALS AND METHODS

2.1. Synthesis. Complexes **1** and **2** were synthesized according to a literature procedure.³² These complexes are highly air-sensitive in solution.

2.2. HFEP Spectroscopy. Neat powder samples were shipped to the National High Magnetic Field Laboratory (NHMFL) in sealed, air-free, round-bottom flasks, which were opened under an inert atmosphere. The HFEP and Mössbauer samples were prepared in a glove box by dispersing ~ 30 mg of each compound in Nujol and holding the mixtures in Delrin and Teflon custom-made containers, respectively. Once removed from the glove box, the samples were stored and handled frozen under liquid nitrogen while being kept at 77 K. The purity and composition of samples used in HFEP were assessed based on the zero-field ^{57}Fe Mössbauer spectra. These complementary measurements allowed us to establish that essentially all iron was found as high-spin Fe^{II} and that Fe^{III} species accounted for less than 2% of the total iron present in the samples. HFEP spectra were obtained using the home-built spectrometer that was previously described⁵⁹ and differs from that description only by the use of a 12–14 GHz source (Virginia Diodes, Charlottesville, VA, USA) complemented by a cascade of multipliers to produce higher frequency harmonics. The experimental results were analyzed (both

Table 1. sH Parameters of 1 and 2 and of Selected Fe^{II}E₄-Containing Systems

complex	D (cm ⁻¹)	E/D	g _x	g _y	g _z	ref
1, [Fe{(SP ⁱ Pr ₂) ₂ N} ₂] ^a	-6.32(1) ^b	0.131(5)	1.997(5) ^b	2.068(5) ^b	2.03(2) ^b	this work
2, [Fe{(SeP ⁱ Pr ₂) ₂ N} ₂] ^a	-4.53(1) ^b	0.194(2)	2.097(5) ^b	2.054(7) ^b	2.19(5) ^{b,c}	this work
Cp-Rd _{red} ^d	5.7(3)	0.25(2)	2.07	2.11	2.00	53
[Fe{(SPPPh ₂) ₂ N} ₂]	9.0 ^b	0.02 ^b	2.10 ^b	2.14 ^b	2.12 ^b	31
[Fe{(SePPh ₂) ₂ N} ₂]	8.22	0.104	2.12	2.12	2.10	23
Rd _{red} ^{a,e}	4.8	0.25	2.1	2.1	2.00	44
Rd _{red} 18-aa model	7.6	0.28	2.11	2.19	2.00	76
(Ph ₄ P) ₂ [Fe(SPh) ₄] ^a	5.84	0.24	2.08	2.08	2.00	43
(Ph ₄ P) ₂ [Fe(SPh) ₄] ^f	5.98	0.24				77
(Ph ₄ P) ₂ [Fe(S ₂ C ₄ O ₂) ₂]	6.93	0.27				8
(Et ₄ N) ₂ [Fe(SR) ₄] ^g	-8.7					9

^aValues determined from the analysis of the HFEPFR spectra. ^bValues obtained from the average of the two distinct sites observed by HFEPFR. ^cThis g_z value is not dependable because of certain assumptions needed to identify the parallel turning points. ^dReduced *Clostridium pasteurianum* Rd. ^eThe specific Rd studied was that from *Pyrococcus abyssi* but expressed in *Escherichia coli* as a triple mutant (Trp4, Arg5, and Ala44 replaced by Leu4, Ser4, and Ser44, respectively). These mutations enhance protein expression, but the Ala44Ser mutation also causes an additional OH bond between Ser44 and the iron-coordinated sulfur of Cys42, which might affect the geometry of the Fe active site, see Barra et al.⁴⁴ ^fValues determined using far-infrared magnetic spectroscopy (FIRMS). ^gR = 2-(Ph)C₆H₄.

simulated and fitted) using the available features of the program SPIN by A. Ozarowski. The analysis used a standard S = 2 sH as expressed in eq 1.

$$\hat{H}_e = \mu_B \vec{B} \cdot \vec{g} \cdot \hat{S} + D[\hat{S}_z^2 - 2 + (\hat{S}_x^2 - \hat{S}_y^2)E/D] \quad (1)$$

2.3. ⁵⁷Fe Mössbauer Spectroscopy. Variable-field, variable-temperature Mössbauer spectra were recorded at temperatures ranging between 4.2 and 200 K and in magnetic fields of up to 8.0 T. The spectra were collected using a constant acceleration spectrometer that was fitted with a Janis 8DT cryostat and an 8.0 T superconducting magnet. The magnetic field was applied parallel to the 14.4 keV γ radiation used to detect the Mössbauer effect. The radiation source consisted of 100 mCi ⁵⁷Co dispersed in a rhodium metal foil. Isomer shifts are quoted relative to the centroid of the iron metal spectrum recorded at room temperature.

The Mössbauer spectra were analyzed in the framework of a standard sH that is described by eq 2a and which is obtained by adding to the electronic sH, eq 1, terms that account for the effects of the ⁵⁷Fe hyperfine interaction, eq 2b.

$$\hat{H} = \hat{H}_e + \hat{H}_{hf} \quad (2a)$$

$$\hat{H}_{hf} = \delta + (eQV_{ZZ}/12)[3\hat{I}_Z^2 - I(I+1) + \eta(\hat{I}_X^2 - \hat{I}_Y^2)] - g_n \beta_n \vec{B} \cdot \hat{I} + \hat{S} \cdot \vec{A} \cdot \hat{I} \quad (2b)$$

The various parameters of eq 2b have their habitual meaning, $\eta = (V_{XX} - V_{YY})/V_{ZZ}$ and $\Delta E_Q = (1/2)eQV_{ZZ}\sqrt{1 + \eta^2/3}$. The relative orientation of the electric field gradient (efg) tensor defined by the (X, Y, Z) coordinates with respect to the (x, y, z) reference frame of the zfs is described by a standard set of Euler angles (α, β, γ). Initial spectral simulations were performed using the WMOSS spectral analysis software developed by Dr. T. Kent (See Co., formerly Web Research Co., Edina, MN). Our simulations were further refined using a modified version of the SPHMOSS (SPinHamiltonianMÖSSbauer) program to account for the orientation-dependent relaxation behavior of complexes 1 and 2.⁶⁰ This latter program was used to explore the zero-field and orientation-dependent relaxational behavior of these compounds.

2.4. Computational Studies. Quantum chemical theory investigations of 1 and 2 were performed using the ORCA 4.0⁶¹ and Gaussian 09⁶² software packages. DFT studies employed the B3LYP,⁶³ BP86,⁶⁴ and TPSSH⁶⁵ functionals in conjunction with Pople's triple- ζ , 6-311G,⁶⁶ and 6-311+G* basis sets.^{67,68} These calculations used both unabridged and simplified structural models derived from the experimental X-ray structures and geometry optimizations.³² The experimental structures contain two sites per

unit cell, labeled site a and site b, corresponding to distinct isomers, see Figure S1 and Tables S1–S3. Regardless of the level of theory, the difference between the self-consistent field (SCF) energies, which are predicted by single point calculations for the individual sites, is less than 1 kcal/mol, see Table S7a. Moreover, calculations performed for the two sites yielded essentially identical results, see Table S7a,b. The simplified structural models were obtained by replacing the ligand's peripheral, P-bonded, ⁱPr groups of site a by Me groups and H atoms, respectively. The influence of these P-bonded groups on the electronic structure of the metal sites was evaluated by monitoring the fine and hyperfine structure parameters predicted at the BP86/6-311G level of theory, see Table S8a,b. Geometry-optimized structures were obtained for symmetrized (*D*₂ point group), Me-substituted, models. These geometries were further optimized in the absence of symmetry constraints (*C*₁ point group). The Cartesian coordinates of the geometry-optimized structures and a summary of selected metric parameters are included in the SI, section S9. The ground state character of the predicted electronic configurations under consideration was confirmed by time-dependent (TD) DFT calculations, which yielded only positive excitations. DFT-predicted zfs and the spin-orbit contribution to hyperfine-structure parameters were obtained using the coupled-perturbed (CP) DFT approach implemented in ORCA.⁶⁹ The influence of a *D*₂ distortion on the electronic structures of 1 and 2 was investigated by using simplified, symmetrized structural models (the *D*₂ point group symmetry of the models used was strictly enforced) to perform relaxed scans of the $\omega_i = E_i - E_0 - E' - P/C$ (*i* = 1–4) dihedral angles at the B3LYP/6-311G level of theory, see Figure 6 and Figure S14. The character of the ground state electronic configurations was assessed by performing Mulliken and Löwdin population analysis.⁷⁰ All single point and geometry optimizations were completed using default convergence criteria.

Ab initio complete active space (CAS) SCF calculations were performed on simplified structural models derived from site a of the crystal structures in which the ⁱPr groups were replaced by Me. These structural models were selected on the basis of CP-DFT calculations performed at the BP86/6-311G level of theory, which showed that replacing the ⁱPr by Me groups leaves the predicted zfs and g-tensors essentially unchanged, see Table S8a. The applicability of this methodology to CASSCF calculations was tested by performing a CAS(5,6) calculation on a model derived from the unabridged experimental structure of 1 (site a), see below. In this case, replacing the ⁱPr groups by Me leads to a minute change in *D* (0.1 cm⁻¹), *E/D* (0.05), and $\Delta g = g - g_e$ values (≤ 0.006), see Table S18. Dynamic correlations were considered using the N-electron valence 2nd order perturbation theory approach, NEVPT2, implemented in ORCA.^{71,72} These calculations used Ahlrichs' triple- ζ , def2-TZVPP basis sets⁷³ in

conjunction with the auxiliary def2/JK basis⁷⁴ and the RI-JK approximation. Initial guesses generated to set up the active spaces of CASSCF calculations were derived from open-shell DFT calculations performed using the BP86/def2-TZVPP functional/basis set combination. The minimal active space, CAS(5,6), of CASSCF(5,6) and CASSCF/NEVPT2(5,6) calculations was spanned by the canonical 3d orbitals of the Fe^{II} ion. The active space of CASSCF(9,14) and CASSCF/NEVPT(9,14) calculations was extended to include the lone pairs of the chalcogen donor atoms. Thus, in addition to the five 3d orbitals of the metal ion (with six electrons), the active space of these calculations included one molecular orbital generated by the linear combination of doubly occupied atomic orbitals enclosing the lone pairs localized on each of the four S/Se atoms (eight electrons total). Computed zfs parameters were obtained using the quasi-degenerate perturbation (QDPT) approach and the effective Hamiltonian protocol implemented in ORCA. The influence of a D_2 distortion on the zfs and efg tensors was assessed using CASSCF(5,6) calculations performed on symmetrized models derived from geometry optimizations performed using DFT at the B3LYP/6-311G level of theory.

3. RESULTS

3.1. HFEP R Spectroscopy. The HFEP R response of complex **1** was weak, and relatively few resonances were observed. Figure 2 (top) shows a spectrum recorded at 406 GHz and 5 K, accompanied by powder-pattern simulations.

The intensity of particular turning points did not correspond to an ideal powder pattern, which could be attributed to some torquing effects persisting despite applying Nujol. Aided by the Mössbauer-obtained sH parameters (*vide infra*), however, it was possible to simulate the spectra quite satisfactorily. Some of the resonances, like the one at ~1.5 T in Figure 2 (top) appeared doubled. Although it is possible that the doubling is an artifact, it could be traced to the presence in **1** of two similar but distinct molecules per unit cell, as demonstrated by X-ray crystallography.³² Simulations show that these sites would have the same D values but differ in E by about 0.045 cm^{-1} .

Despite the limited number of resonances, it was possible to generate a 2D field/frequency map and thus determine accurately the sH parameters using the tunable-frequency approach.⁷⁵ Whenever a given resonance was doubled, an average value was used in the computer fits. The field/frequency map of resonances is shown in Figure 3 (top), along with the simulations using the best-fitted sH parameters, as listed in Table 1. It should be stressed that the sH parameters obtained this way are frequency-independent and thus superior to those from single-frequency spectra.

The HFEP R response of complex **2** was stronger than that of **1**. Figure 2 (bottom) shows a spectrum of **2** recorded at 406 GHz and 10 K, along with simulations assuming a random distribution of crystallites in space. The experimental spectrum is accompanied by its simulations, which used sH parameters obtained from Mössbauer experiments. A comparison of simulations with experiments shows that (a) the powder pattern is fairly well reproduced, (b) the zfs parameter D is negative, and (c) some of the turning points appear doubled, analogously to complex **1**. We assume that the doubling originates from two similar but slightly different $S = 2$ species exhibiting the same D but differing in E by of about 0.05 cm^{-1} , as indicated by the crystal structure.

The sign of D in **2** was confirmed by a temperature dependence of the 203 GHz spectrum as shown in Figure S3 in the SI. The observed changes in the intensity of particular

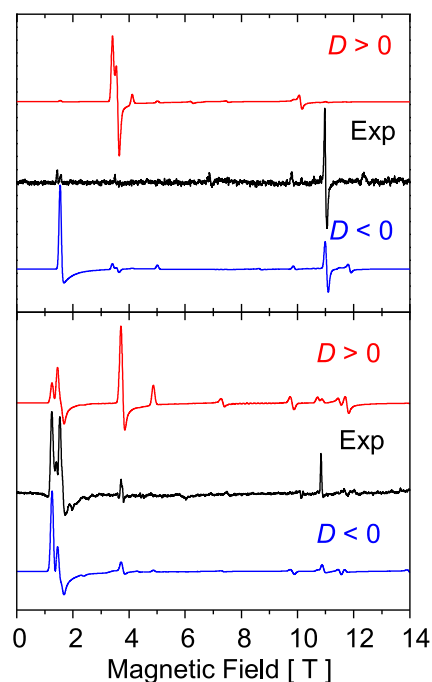


Figure 2. (top) A 406.4 GHz EPR spectrum of **1** at 5 K (black trace) accompanied by powder-pattern simulations using the following absolute values of zfs parameters: $|D| = 6.35\text{ cm}^{-1}$, $|E/D| = 0.121$, and $g = [2.02, 2.07, 2.03]$. Red trace: positive D ; blue trace: negative D . The doubling of the low-field (1.5 T) parallel turning point is not reflected in the simulations; it could be simulated by two sets of parameters differing by a small value of $|E/D|$ (~ 0.007). The intensity ratio of the two dominant turning points at ~ 1.5 and 11 T does not quite correspond to the powder pattern simulations, indicative of torquing effects; however, the pattern is closer to the negative D case than positive D ; (bottom): 406.4 GHz EPR spectrum of **2** at 10 K (black trace) accompanied by powder-pattern simulations using the absolute values of sH parameters as in Table 1. Red trace: positive D ; blue trace: negative D . The structure on top of the two low-field (1.5 T) resonances is not fully reflected in the simulations; it could be simulated by two sets of parameters differing by a small value of E/D (~ 0.01). The increased amplitude of the 10.8 T perpendicular turning point relative to the simulations is indicative of torquing effects.

turning points are interpreted in terms of the sign of D in Figure S4 in the SI and its caption.

The observed resonances were collected in a two-dimensional field/frequency map, along the procedure of tunable-frequency EPR,⁷⁵ shown in Figure 3 (bottom). Computer fits of the sH parameters used values obtained from the Mössbauer experiment as seeds and resulted in the data shown in Table 1. Note that only one averaged set of the two observed sets of resonances was used in the fits, similarly to the procedure employed to analyze the data recorded for complex **1**.

3.2. ⁵⁷Fe Mössbauer Spectroscopy. To assess the electronic structure of complexes **1** and **2**, a series of field- and temperature-dependent ⁵⁷Fe Mössbauer spectra of ground polycrystalline samples were recorded at fields up to 8 T and temperatures between 4.2 and 200 K. At zero field, the spectra of **1** and **2** exhibit two well-defined resonances, i.e., quadrupole doublets, and are characterized by an isomer shift $\delta \approx 0.8\text{ mm/s}$ and a quadrupole splitting $|\Delta E_Q| > 3.0\text{ mm/s}$, see Table 2 and Table S5. These values are typical of tetrahedral Fe^{II} sites (Table 2).⁷⁸ While the isomer shift values exhibit a slight temperature dependence, which can be traced to a second-order Doppler effect, the quadrupole splitting

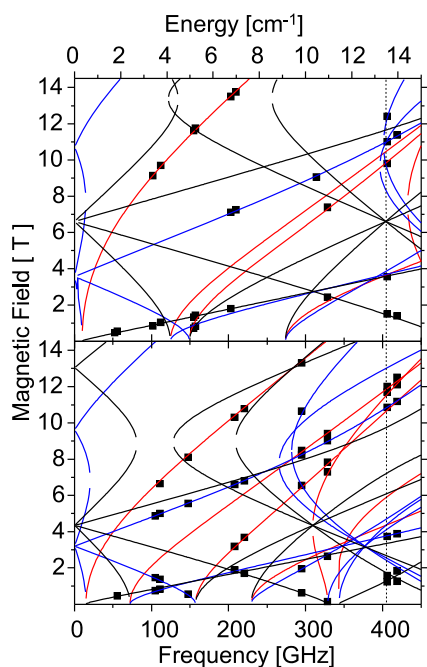


Figure 3. 2D field vs frequency (or energy) map of EPR resonances in **1** (top) and **2** (bottom) at 5 K. The squares represent either the experimental resonances or the averaged position of those resonances that were doubled (see Figure 2). Curves were simulated using best-fitted sH parameters as in Table 1. Red traces: turning points with magnetic field B_0 parallel to the x axis of the zfs tensor; blue, $B_0 \parallel y$; black, $B_0 \parallel z$. at 10 K. Squares represent either the observed resonances or the averaged positions of those resonances that were doubled). Curves were simulated using best-fitted sH parameters. The dashed vertical line represents the frequency at which the spectra shown in Figure 2 were recorded.

values are nearly temperature-independent, see Table S5. Inspection of Figure 4 and Figures S5 and S6 (SI) reveals at 4.2 K an abrupt increase in the magnetic hyperfine splitting such that it has reached a saturation value at only 1 T. This field-dependent behavior is due to a negative zfs parameter D for **1** and **2**, which leads to a ground quasi-doublet with a relatively small zfs ($\delta_{zfs} \approx 0.3 - 0.5 \text{ cm}^{-1}$, see below) that is easily overwhelmed by the Zeeman interaction when the field is aligned with the molecular z -axis, see Figure S8, left. At higher temperatures, a Curie-like behavior is anticipated such that thermally averaged spin expectation value $\langle \hat{S} \rangle_{th} \approx 1/T$, see Figure S8, right. Under these conditions, the hyperfine splitting pattern of the field-dependent spectra is essentially independent

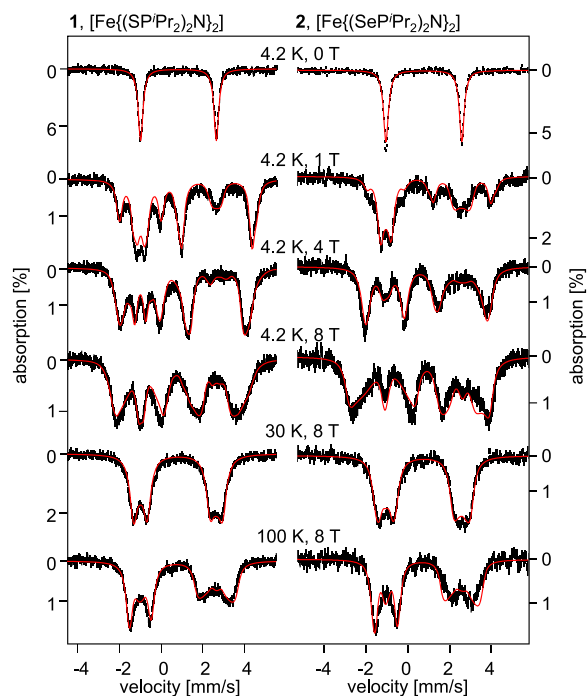


Figure 4. Selected field-dependent ^{57}Fe Mössbauer spectra recorded for complex **1** (left) and **2** (right). The solid red lines are simulations obtained using the zfs parameters listed in Table 1 and hyperfine splitting parameters listed in Table 2. The simulations of the field-dependent 4.2 K spectra were obtained using an orientation-dependent relaxation model, see text.

ent of zfs and is dominated by the nuclear Zeeman and quadrupolar interactions. Consequently, analysis of the high-field, high-temperature spectra allowed us to establish the asymmetry parameter of the efg tensor, and that the ΔE_Q of **1** and **2** is positive.

The crystallographic characterization of **1** and **2** revealed that the $\text{Fe}^{\text{II}}\text{E}_4$ cores exhibit an almost ideal D_2 point group symmetry.³² Because D_2 -symmetric metal sites have three orthogonal C_2 axes, all tensors were expected to be collinear. While this assumption was verified by the analysis of the field-dependent Mössbauer spectra of **1**, our analysis for **2** suggested the presence of a relatively small, $\beta \approx 10^\circ$, rotation around the y axis of the efg tensor with respect to the zfs reference frame.

The magnitude of the observed magnetic hyperfine splitting pattern is determined by the effective magnetic field which acts on the ^{57}Fe nuclei. This field originates from the vector sum of the internal and applied fields, $\mathbf{B}_{\text{effective}} = \mathbf{B}_{\text{internal}} + \mathbf{B}_{\text{applied}}$, where

Table 2. Hyperfine Parameters of **1** and **2** and Related Systems

complex	δ^a (mm/s)	ΔE_Q^a (mm/s)	η	$A_x/g_n\beta_n$ (T)	$A_y/g_n\beta_n$ (T)	$A_z/g_n\beta_n$ (T)	ref.
1 , $[\text{Fe}\{(\text{SP}^{\text{Pr}})_2\text{N}\}_2]$	0.82(1)	3.62(1)	0.6(2)	−19(1)	−22(1)	−5.8(8)	this work
2 , $[\text{Fe}\{(\text{SeP}^{\text{Pr}})_2\text{N}\}_2]$	0.78(1)	3.61(1)	0.4(2) ^b	−15.8(6)	−21.0(8)	−5.5(6)	this work
$[\text{Fe}\{(\text{SePPh}_2)_2\text{N}\}_2]$	0.79	3.23(1)					23
$[\text{PPh}_4]_2[\text{Fe}(\text{SPh})_4]$	0.66 ^c	−3.24	0.67	−14.8	−8.1	−24.7	7
$\text{Cp-Rd}_{\text{red}}^c$	0.70	−3.25	0.75	−14.5	−8.2	−24.17	53
Rd_{red} 18-aa model	0.69	−3.24	0.84	−18.8	−8.3	−33	76
$[\text{Fe}(\text{S}_2\text{-o-xy})_2]^{2-d}$	0.61	−3.32					14

^aValues determined from the analysis of the 4.2 K, 0 T spectra. For the values observed at other temperatures, see Table S5. ^bThe efg tensor was found to be rotated from the reference frame of the zfs tensor. This rotation is quantified by the $\alpha = \gamma = 0^\circ$ and $\beta = 10(10)^\circ$ set of Euler angles. ^cValue quoted at 4.2 K. However, this value is listed as 0.73(2) mm/s in Table 1 of ref 53. ^dValues determined at 1.4 K for $\text{Na}(\text{Ph}_4\text{As})[\text{Fe}(\text{S}_2\text{-o-xy})_2]$.

$\vec{B}_{\text{internal}} = -\tilde{A} \cdot \langle \hat{S} \rangle / g_n \mu_n$. The spin expectation values, $\langle \hat{S} \rangle$, are dependent on the specifics of the fine structure of the $S = 2$ spin ground state, i.e., zfs and g tensors. Our initial investigations of the Mössbauer spectra allowed us to assess the magnitude of the zfs. These estimates were subsequently refined by analyzing the field/frequency dependencies of the observed HFEPR resonances, *vide supra*.

Together with the successful simulations of the individual HFEPR spectra, this procedure allowed us not only to determine the values of the zfs parameters D and E , with exquisite precision, but also to establish that the parameter set for each of these two complexes is indeed unique. Our investigation revealed that for **1** and **2**, the zfs tensors are rhombic and D is negative, in contrast to the D of Rd_{red} which is positive, see Table 1. The negative D leads to a ground state consisting of an isolated quasi-doublet $|2\pm\rangle \approx (|2,2\rangle \pm |2,-2\rangle) / \sqrt{2}$, for which the two levels are separated by an energy gap: $\delta_{zfs} \approx 3 \cdot D \cdot (E/D)^2 \approx 0.31 \text{ cm}^{-1}$ for **1** and 0.49 cm^{-1} for **2**. The applied field induces the mixing of these levels leading to states that are essentially magnetically uniaxial, with the easy axis found along z , that is, $\langle \hat{S}_z \rangle \gg \langle \hat{S}_x \rangle \approx \langle \hat{S}_y \rangle \approx 0$, and for $B \geq 0.5 \text{ T}$, $\langle \hat{S}_z \rangle \cong -2$, $B_{\text{int},z} = -2A_z / g_n \mu_n$, see Figure S8. Consequently, the 4.2 K spectra are sensitive to the A_z component of the hyperfine coupling tensor A . The remaining A tensor components were determined from the analysis of the 8 T temperature-dependent spectra.

Inspection of the low-field, $B < 4.0 \text{ T}$, 4.2 K spectra reveals the presence of two distinct spectral components, see Figure 4 and Figures S5–S7 (SI). This observation was rationalized by considering the presence, for these experimental conditions, of an orientation-dependent spin–lattice relaxation. Such a behavior was first described by Zimmerman *et al.*⁷⁹ and more recently by one of us.⁸⁰ Thus, the component with a larger hyperfine splitting accounts for a fraction of molecules for which the flip rate of the electronic spin is smaller than 10^5 s^{-1} , i.e., those that are in a slow relaxation regime. In contrast, the component with the smaller hyperfine splitting originates from a fraction of molecules for which the electronic spin is in a fast relaxation regime, that is, a spin flip rate larger than 10^7 s^{-1} , see Figure S7. The simulations of the 4.2 K spectra of **1** and **2** were obtained using an orientation-dependent relaxation rate. The partition of the Fe^{II} sites in fractions that exhibit either a slow or fast relaxation regime was accomplished considering the energy difference between the two lowest spin sublevels. The negative D values of **1** and **2** lead to ground quasi-doublets that exhibit a considerably larger Zeeman splitting when the field is applied along z than when it is found in the xy plane. The effective g values of the ground quasi-doublet are $g_{\text{eff},z} \approx 8.1 \gg g_{\text{eff},xy} \approx 0.5$. For each field magnitude and field orientation, we define either a fast or a slow relaxation regime if the combined zfs and Zeeman splitting is respectively smaller or larger than a numerical value Δ_{relax} . Thus, for a powder average, molecules that have their molecular z -axis roughly aligned with the applied field adopt a slow relaxation regime. In contrast, molecules with orientations for which the applied field lies roughly in the xy plane of their zfs tensor adopt a fast relaxation regime. Increasing the field leads to an increase in the fraction of fast-relaxing “perpendicular” molecules at the expense of the slow relaxing “parallel” fraction. Simulations of the 4.2 K spectra of **1** were obtained using $\Delta_{\text{relax}} \approx 1.5(5) \text{ cm}^{-1}$. For **2**, simulations of the low temperature (4.2 K) spectra were obtained by modulating the Δ_{relax} value such that a quarter of the total number of

molecules were slow relaxing. At temperatures of $>4.2 \text{ K}$, the simulations were obtained assuming entirely a fast relaxation regime. Finally, the spectral simulations presented here are compromises that fit best the entire data set using the zfs and g tensors determined from HFEPR and a single set of hyperfine splitting values, which are listed in Table 2.

4. DISCUSSION

4.1. Crystal-Field Analysis of the sH Parameters. The signs of ΔE_Q and D of pseudo-tetrahedral $S = 2$, Fe^{II} -thiolato complexes have been correlated with the electronic configuration of their ground state.⁵³ Thus, a negative ΔE_Q and positive D , as experimentally determined in $\text{Cp Rd}_{\text{red}}$ (see footnote d of Table 1), are indicative of a doubly occupied d_z^2 orbital, whereas a positive ΔE_Q and negative D suggest a doubly occupied $d_{x^2-y^2}$ orbital. For T_d complexes, the d_z^2 , $d_{x^2-y^2}$ orbitals span the e manifold and for D_2 , they both have a_1 character, thus their mixing is symmetry-allowed. Therefore, for **1** and **2**, which have an approximate D_2 symmetry, the Fe^{II} 3d orbital associated with the ground state, $|GS\rangle$, is best described considering a linear combination, such that

$$|GS\rangle = \alpha d_z^2 + \beta d_{x^2-y^2} \quad (3)$$

where α and β are linearly dependent mixing coefficients. These coefficients are often correlated with specific structural parameters such as the $\omega_i = E_i - E' - P$ dihedral or torsion angle of **1** and **2**, *vide infra*. Although this is a simplification, to avoid overparameterization, in this analysis, we assume isotropic π -bonding. While the spin–orbit coupling (SOC) interaction mixes the ground-state with the excited 5T_2 orbital states for which the single spin-down β electron occupies one of the $t_2 [d_{xy}, d_{xz}, d_{yz}]$ orbitals, due to the $\Delta m_L = 0, \pm 1$ selection rules, the ground orbital state does not interact with the excited state of the 5E manifold. These interactions determine the g tensor, dominate D , and give rise to large orbital contributions to the A tensor. Using the second order perturbation theory, the contributions of the excited quintet states to these parameters may be expressed as

$$g_{ij} = g_e \delta_{ij} - \lambda \Lambda_{ij} \quad (4)$$

$$D_{ij} = -\lambda^2 \Lambda_{ij} \quad (5)$$

$$A_{L,ij} = -P \lambda \Lambda_{ij} \quad (6)$$

where $i, j = x, y, z$ and

$$\Lambda_{xx} = \frac{(\sqrt{3}\alpha + \beta)^2}{\epsilon(d_{yz})} \quad (7a)$$

$$\Lambda_{yy} = \frac{(\sqrt{3}\alpha - \beta)^2}{\epsilon(d_{xz})} \quad (7b)$$

$$\Lambda_{zz} = \frac{4\beta^2}{\epsilon(d_{xy})} \quad (7c)$$

The D tensor predicted using eq 5 is not traceless, and it accounts for only the contributions of the excited state with the same spin as the ground state. The D and E/D values incorporated into the second term of eq 1 are obtained after converting the resulting zfs tensor to its traceless form. Equation 6 lists only the orbital contributions to the A tensor. The complete A tensor also includes contribution from the

Fermi contact term (A_{FC}) and spin-dipolar term (A_{SD}). The expressions of the A tensor components are listed in the SI, see eq S1a–c. Finally, λ represents the multi-electron, LS , SOC constant and $P = 2g_n\beta_n\langle r^{-3} \rangle$ is a scaling constant.

For both **1** and **2**, $\Delta E_Q > 0$ and $D < 0$ which suggests that $\alpha \approx 0$ and $\beta \approx 1$. Inspection of Tables 1 and 2 suggests that the A values of **1** and **2** and the g values of **2** further corroborate this conclusion. Thus, for $\alpha \ll \beta \approx 1$ eqs 7a–c predict that when $\varepsilon(d_{xz}) \approx \varepsilon(d_{yz}) \approx \varepsilon(d_{xy})$, $g_x \approx g_y < g_z$ and $|A_x| \approx |A_y| \gg |A_z|$. By setting the coefficients of eqs 7a–c as $\alpha = \cos \theta$ and $\beta = \sin \theta$, see Figure S9, we recover the expressions for the spin–quintet contributions to the hyperfine splitting parameters first provided by Bertrand and Gayda, see eq S1a–c in the SI.^{81,82} Analogous expressions for the g values were derived by Abragam and Bleaney, see eq S2a–d in the SI.⁸³ However, the inspection of Figures S10 and S11 shows that even for relatively moderate θ or β values, such as those expected for a mixed ground state with a dominant $d_{x^2-y^2}$ character, the perturbation theory expressions derived for the asymmetry parameters of the efg and zfs tensors, eqs S3 and S4 in the SI, lose their usefulness. To obtain an initial estimate of the mixing coefficients, we have evaluated these parameters using eqs 8 and 9. These are periodic functions, $\nu = 12$, which not only provide an estimate of η and E/D ,⁸⁴ but also confine their values to $0 \leq \eta \leq 1$ and $0 \leq E/D \leq 1/3$, as expected when the efg and zfs tensors are expressed in their proper frame of reference, see Figures S10 and S11.

$$\eta = \frac{1}{2}(|\sin 6\theta| - |\cos 6\theta| + 1) \quad (8)$$

$$E/D = \frac{1}{6}(|\sin 6\theta| - |\cos 6\theta| + 1) \quad (9)$$

Because the efg is a ground state property, the periodicity of the $\eta(\theta)$ function is not affected by the difference in the energies of the individual excited orbital states with a 5T_2 parentage. In contrast, the $E/D(\theta)$ function loses its 12-fold character when the t_2 orbital energies are unequal, $\varepsilon(d_{xz}) \neq \varepsilon(d_{yz}) \neq \varepsilon(d_{xy})$, with its behavior becoming more complex, see Figure S12. These expressions suggest that for equal orbital energies, η and E/D should exhibit a 3:1 ratio and an identical dependence on the mixing parameter θ , see Figure 5 and Figure S13.

Because the experimental values of E/D and η do not conform to the theoretical 1/3 ratio, eqs 8 and 9 can be used, at best, to limit the range of likely θ values. Figure 5 shows that there are six intervals, which are highlighted in blue, that minimize the difference between the experimental values and theoretical η and E/D , see Table S6. However, for complex **1**, the contribution of the $d_{x^2-y^2}$ to the ground state, which is determined by the square of the β linear coefficient, shown in black, is maximized for only a non-contiguous range spanning $\sim 5.6^\circ$ for which $81^\circ < \theta < 99^\circ$, see Table S6. The results of the analogous analysis performed for **2** are presented in Figure S13 and Table S6.

For pseudotetrahedral tetrathiolato Fe^{II} sites with a d_z^2 ground state, such as that of $Cp\text{-Rd}_{\text{red}}$, the null matrix element, $\langle d_z^2 | \hat{L}_z | \text{ES} \rangle = 0$ ($\text{ES} = \text{d}$ orbital, excited states), leads to $\Lambda_{zz} = 0$ and a quenched spin–orbit contribution along z , i.e., $g_z \approx g_e$ and $A_z \approx A_{FC}$, where $A_{FC} = -Pk$. In contrast, for compounds with a $d_{x^2-y^2}$ ground state, the $\langle d_{x^2-y^2} | \hat{L}_z | d_{xy} \rangle = -2i$ matrix element being twice as large as $\langle d_{x^2-y^2} | \hat{L}_x | d_{yz} \rangle = \langle d_{x^2-y^2} | \hat{L}_y | d_{xz} \rangle = i$, leads to $\Lambda_{zz} \approx 4\Lambda_{xx} \approx 4\Lambda_{yy}$ such that the largest

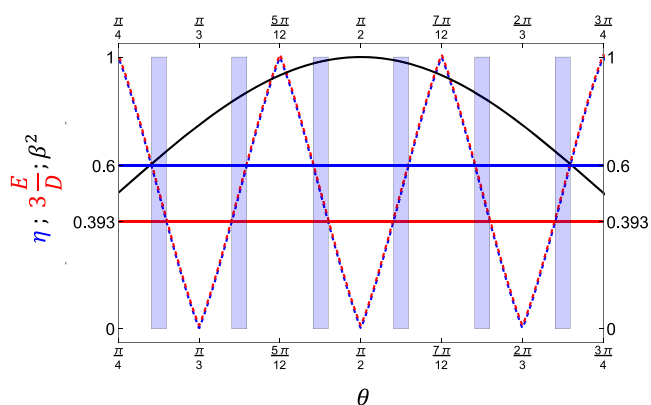


Figure 5. Theoretical E/D (dashed red, multiplied by 3) and η (dashed blue) values derived using eqs 8 and 9, used to estimate the mixing parameter θ of **1**. Shown in black is the contribution of $d_{x^2-y^2}$ to the ground state, that is, the square of the β coefficient included in eq 1. The horizontal lines are the experimental values of η (blue) and three times the E/D (red) value obtained for **1**. The blue rectangles highlight the ranges of θ values, which minimize the discrepancy between the experimental and theoretical values.

spin–orbit contribution is observed along z , even when d_{xy} has the highest orbital energy of the t_2 subset, *vide infra*. Inspection of Table 2 shows that, consistent with the presence of a large positive orbital contribution along z , the A tensors of **1** and **2** exhibit A_z values that have a much lower magnitude than the other two A tensor components. However, the g_z value of **1** is not consistent with the expected $\Delta g_z \gg \Delta g_x \approx \Delta g_y$ pattern, suggesting that for this complex, either this model is not valid or that the experimental g values are not reliable. To obtain experimental estimates of not only θ but also of P , κ , λ , $\varepsilon(d_{xz})$, $\varepsilon(d_{yz})$, and $\varepsilon(d_{xy})$ for **1**, we have minimized the differences between the experimental and theoretical A , η , and E/D values. Considering a single energy value for the orbitals of the t_2 subset and minimizing discrepancies in a stepwise fashion, we find that the experimental A tensor and the E/D ratio of **1** are well reproduced by using $\theta = 83.5^\circ$, $\varepsilon = 4300 \text{ cm}^{-1}$, $\kappa = 0.42$, and $\lambda = -82 \text{ cm}^{-1}$, and $P = 45 \text{ T}$. While the theoretical $\eta \cong 0.4$ parameter obtained using these parameters is at the lower limit of the experimental range, the use of dissimilar orbital energies does not lead to better agreement. The predicted g values, $g_x = 2.056$, $g_y = 2.026$, and $g_z = 2.153$, lead to $g_{\text{av}} = 2.078$, which is higher than the $g_{\text{av}} = 2.03(1)$ experimental value. However, considering the modest quality of the experimental HFEP spectra, this mismatch is acceptable, as the data quality affects much more the g values than the zfs.

Following the procedure described above, we find that the experimental values of not only the A tensor components, η , and E/D but also of the g values of **2** are well reproduced using $\theta = 83.6^\circ$, $P = 44 \text{ T}$, $\kappa = 0.42$, $\lambda = -83 \text{ cm}^{-1}$, $\varepsilon(d_{xz}) = 1960 \text{ cm}^{-1}$, $\varepsilon(d_{yz}) = 2570 \text{ cm}^{-1}$, and $\varepsilon(d_{xy}) = 3910 \text{ cm}^{-1}$. The P , κ , and λ values obtained for **1** and **2** are consistent with those derived in previous studies for the iron–sulfur site of $Cp\text{-Rd}_{\text{red}}$: $P = 46 \text{ T}$, $\kappa = 0.40$, and $\lambda = -87.5 \pm 5 \text{ cm}^{-1}$.⁵³ By taking the average of the experimental A values, we obtain the isotropic part of the hyperfine coupling tensor, which for **2**, yields $A_{\text{iso}} = -14.1 \text{ T}$. This value accounts for the combined contribution of the Fermi–contact term, A_{FC} , and the pseudo-contact, orbital contribution, A_{pseudo} . The latter value is estimated from the g values, $A_{\text{pseudo}} = \frac{1}{3}P \text{Tr}(\mathbf{g} - g_e) = 4.9 \text{ T}$, which yields $A_{FC} = A_{\text{iso}} - A_{\text{pseudo}} = -19.0 \text{ T}$. By subtracting from the experimental

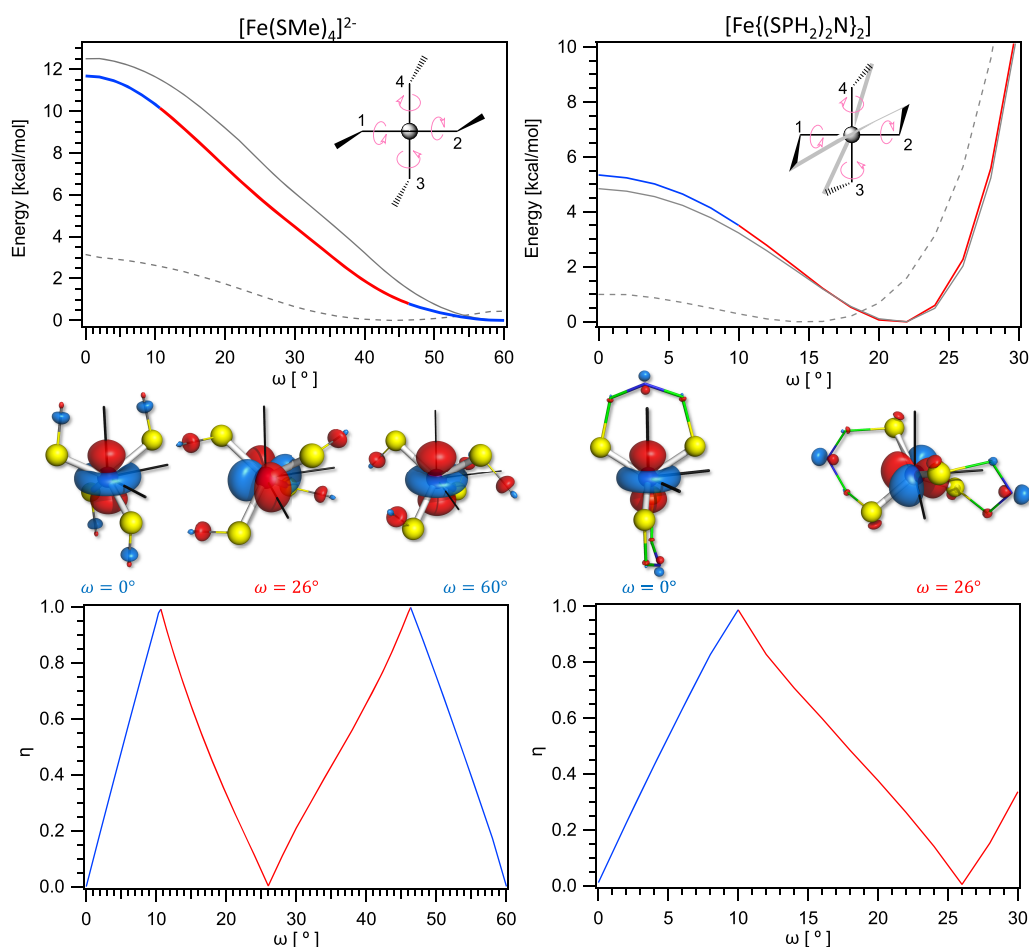


Figure 6. (top) Potential energies of $[\text{M}^{\text{II/III}}(\text{SMe})_4]^{2-/-}$ (left) and $[\text{M}^{\text{II/III}}\{(\text{SPH}_2)_2\text{N}\}_2]^{0/+}$ (right) as function of the D_2 distortion angle ω . At $\omega = 0, 60^\circ$ these models have a D_{2d} and for all other ω values, they have a D_2 symmetry. Shown in red/blue are the energies predicted for $M = \text{Fe}^{\text{II}}$, those obtained for $M = \text{Zn}^{\text{II}}$ are shown in gray, and those shown using a dashed line are obtained for $M = \text{Fe}^{\text{III}}$. (middle) Doubly occupied metal $3d$ orbitals of the Fe^{II} models obtained at ω values for which the DFT-predicted $\eta \approx 0$. The coordinate axes shown in black indicate the frame of the efg tensor with the z -axis taken in the vertical direction. (bottom) DFT-predicted asymmetry parameter η vs the D_2 distortion angle ω . For both the potential energy and η plots, shown in red are the ω values for which the contribution of the $d_{x^2-y^2}$ orbital is dominant ($\Delta E_Q > 0$) and in blue are the regions for which the contribution of the d_z^2 is dominant ($\Delta E_Q < 0$). These results were obtained at the B3LYP/6-311G level of theory.

values, the combined contribution of the contact and orbital terms, we determined the spin-dipolar (SD) contribution $A_{\text{SD},x} = -0.97$ T, $A_{\text{SD},y} = -4.27$ T, $A_{\text{SD},z} = +5.24$ T. The asymmetry parameter of the spin-dipolar A tensor $\eta_{\text{A}_{\text{SD}}} = |A_{\text{SD},y} - A_{\text{SD},x}| / A_{\text{SD},z} = 0.63$ is, within experimental error, similar to that of the experimental efg tensor $\eta = 0.4(2)$, suggesting that the efg tensor of **2** is dominated by the valence contribution. One interesting feature of the A_{SD} tensor, also reflected by the theoretical A_{SD} tensor obtained using the parameters listed above and the second terms of eq S1a–c in the SI, $A_{\text{SD},x} = -1.85$ T, $A_{\text{SD},y} = -4.27$ T, $A_{\text{SD},z} = +6.13$ T, is that its largest component is parallel to the largest orbital contribution. This alignment of the two largest positive contributions to the A tensor nearly cancels the large negative Fermi contact along the z direction.

The SOC constants, θ values, and the orbital energies derived above may be used to estimate the excited quintet states' contribution to D . Substituting these values in eq 5, we obtain $D = -4.57$ cm^{-1} for **1** and $D = -3.94$ cm^{-1} for **2**, which account for only 72 and 87% of the experimental value, respectively. The mismatch might be traced to spin–spin

coupling (SSC), to the contribution of triplet states to the zfs, or to a combination of both.

$$D_{\text{SSC}} = 3\rho \cos 2\theta \quad (10)$$

In comparison, for the C_p - Rd_{red} site, Vrajmasu et al. estimated that 42% of the experimental value, $D = +5.7$ cm^{-1} , originates from the contribution of triplet states and 7% is due to SSC.⁵³ For $[\text{Fe}(\text{SPhC}_6\text{H}_4)_4]^{2-}$, which like **1** and **2** has a negative D , Gebhard et al. estimated that 25% of the experimental $D = -8.7$ cm^{-1} value originates from SOC contribution of the excited triplet states.⁹ Using eq 10 and the SSC constant derived by Watson and Blume from atomic Hatree–Fock calculations, $\rho = 0.18$ cm^{-1} , we estimate that the SSC contribution to the zfs of **1** and **2** is relatively modest, $D_{\text{SSC}} \cong -0.53$ cm^{-1} . These arguments suggest that while for **1** the interaction with the triplet states accounts for $\sim 20\%$ of the zfs, $D_{S=1} = -1.22$ cm^{-1} , for **2**, this contribution is essentially null, $D_{S=1} = -0.06$ cm^{-1} .

4.2. DFT-Predicted Ground State Electronic Configurations and Electric Field Gradients. The geometric distortions of four-coordinate iron–sulfur sites have been analyzed by inscribing their first coordination sphere into a cube or a rectangular parallelepiped, see Figure S2. For

tetrahedral (T_d) sites, the edges of the parallelepiped are equal, $a = b = c$, and the S–Fe–S bond angles are 109.5° . However, typical iron sulfur sites are distorted, most often exhibiting an approximate D_{2d} symmetry obtained by either compressing, $a < b = c$, or elongating the cube, $a > b = c$. While for a compressed structure we observe four smaller and two larger S–Fe–S bond angles, for an elongated structure, we expect four larger and two smaller angles. Because a compression pushes the S-containing ligands away from the z -axis, defined as parallel to the direction of the distortion, toward the xy plane, the $d_{x^2-y^2}$ orbital is destabilized and we anticipate a d_{z^2} -type ground state. In contrast, for an elongated structure, the ligands are brought closer to the z -axis destabilizing the d_z^2 orbital and yielding a $d_{x^2-y^2}$ -type ground state. Inspection of Table S3a,b shows that for **1** and **2**, we observe structures elongated along an axis perpendicular to that bisecting the $\{(\text{EP}^{\text{Pr}})_2\text{N}\}^-$ ligands. Thus, two E–E interligand distances are ~ 0.16 Å (0.27 Å) shorter for **1**(**2**) than the four other inter- and intraligand E–E distances. Similarly, two E–Fe–E interligand bond angles are $\sim 7^\circ$ (11°) smaller than the two sets of inter- and intraligand bond angles, see Tables S1–S4.

The $d_{x^2-y^2}$ ground state inferred from the signs of D and ΔE_Q is further corroborated by the crystal-field analysis of the first coordination spheres of **1** and **2**. However, our DFT and CASSCF calculations, *vide infra*, predict that, regardless of the method used, the large positive component of the efg tensor, that is the z -axis, is not aligned with the S_4 improper rotation axis of the D_{2d} idealized FeE_4 core, denoting the direction along which the core is tetragonally elongated from T_d symmetry, rather it is orthogonal to the S_4 axis and it bisects the two large E–Fe–E intraligand bond angles, see Figure S2. While this mismatch seems minor, it indicates that the crystal field analysis of only the first coordination sphere is not enough to rationalize the electronic structure of **1** and **2** and that additional factors need to be considered. Our observations are not unprecedented. Although the coordination spheres of $Cp\text{-Rd}_{\text{red}}$ and of $[\text{Fe}(\text{SPh})_4]^{2-}$ are elongated, like those of **1** and **2**, unlike our compounds, they have a negative ΔE_Q and a d_z^2 ground state opposite from that expected based on the distortion of their FeS_4 cores.

Several authors, starting with Bair and Goddard,⁸⁵ have rationalized the electronic structure of iron–sulfur sites by considering the influence of the $\omega_i \equiv \text{C}-\text{S}_i-\text{Fe}-\text{S}'$ torsion angles.⁸⁶ These dihedral angles account for the rotation of the C–S_{*i*} bonds around the Fe–S' axes and direct the orientation of the S_{*i*} ($i = 1-4$) sulfur lone pair(s). Therefore, these angles control the anisotropic π interactions between the sulfur ligands and the central metal ion and modulate the energies of iron 3d orbitals. The $[\text{Fe}(\text{SCH}_3)_4]^{2-}$ anion may be used to model the structures of both $Cp\text{-Rd}_{\text{red}}$ and complexes **1/2**, see Figure S14. This model may adopt two high-symmetry, D_{2d} structures, one that for $\omega_i = 60, 180^\circ$ ($i = 1-4$), approximates the sites of $Cp\text{-Rd}_{\text{red}}$ and $[\text{Fe}(\text{SPh})_4]^{2-}$, and another that for $\omega_i = 0, 120^\circ$, approximates the structures of **1** and **2** as well as of the Holm–Ibers complex, $[\text{Fe}(\text{S}_2\text{-}o\text{-}xyl)_2]^{2-}$. The symmetry of **1** and **2** is lower than D_{2d} and is consistent with a distortion along a D_2 coordinate for which $\omega \equiv \omega_1 = \omega_2 = \omega_3 = \omega_4 > 0$. Although varying ω from 0 to 60° interconverts the two high-symmetry D_{2d} structures, see Figure 6 and Figure S14, this distortion is different from that observed for $Cp\text{-Rd}_{\text{red}}$. For the latter case, the $[\text{Fe}(\text{SC})_4]$ core adopts a “double-bird” configuration for which, at $\omega \approx 180^\circ$, the two “birds” are interchanged by an S_4 symmetry operation. However, the

approximate C_2 symmetry of the rubredoxin's site is lower than D_{2d} and is rationalized by considering a torsion around the C_2' axis perpendicular to the S_4 axis of the D_{2d} core such that $\omega_1 \approx \omega_3 \approx \omega$ and $\omega_2 \approx \omega_4 \approx 0$.

We have used DFT to analyze the influence of a distortion along the D_2 coordinate on the electronic structure of $[\text{Fe}^{\text{II}}(\text{SMe})_4]^{2-}$ and $[\text{Fe}^{\text{II}}\{(\text{SPH}_2)_2\text{N}\}_2]$, which is a simplified model for **1** and **2**, see Figure 6. The effects on the electronic structure of $[\text{Fe}(\text{SR})_4]$ models of distortion along a S_4 coordinate, $\omega \equiv \omega_1 = \omega_2 = -\omega_3 = -\omega_4$ (see Figure S14), have been analyzed in detail by Vrajmasu et al.⁸⁷ Although the lowest minima of the $\text{Fe}(\text{SC}_\beta)_4$ core are expected to have an S_4 symmetry, the chelating character of the bidentate disulfido-imidodiphosphinato ligands of **1** and **2** imposes a distortion along the D_2 coordinate. Because they belong to different representations of the D_{2d} group, for $\omega = 0, 60^\circ$, the mixing of $d_{x^2-y^2}$ with d_z^2 is not allowed. For other values, ω mixes these two orbitals, in a fashion analogous to that described above, inducing a changeover from a d_z^2 ground state, observed for D_{2d} configurations, to a $d_{x^2-y^2}$ ground state at intermediate $\omega \approx 26^\circ$ values, see Figure 6 middle. Although varying ω from 0 to 60° leads to an interconversion of the two D_{2d} forms, this change is concomitant with a rotation of the z -axis with respect to the FeE_4 core. Inspection of Figure S14 shows that the original orientation of the z -axis is recovered only after a complete $\omega = 0 \rightarrow 180^\circ$ rotation. Because for $\omega = 0$ and 120° , the C_β groups are at their closest approach, these D_{2d} conformations of $[\text{Fe}(\text{SMe})_4]^{2-}$ are destabilized by ~ 12 kcal/mol with respect to the “double-bird” analogues observed at $\omega = 60$ and 180° . In contrast, the bidentate, chelating $\{(\text{SPH}_2)\text{N}\}^-$ ligand impedes a complete 180° rotation along the same D_2 coordinate and leads to a minimum at $\omega \approx 22^\circ$. Although the $\omega_{\text{av}} \approx 17.1^\circ$ (16.7°) experimental values determined for **1**(**2**) are smaller than those derived for the simplified models, they are in the range of ω values for which a $d_{x^2-y^2}$ ground state is predicted. Interestingly, these calculations also elucidate the origin of the seeming disparity between the d_z^2 ground state of the Holm–Ibers complex and those of **1** and **2**. Although all three complexes are supported by bidentate, chelating ligands that lock the geometries of their Fe^{II} sites into similar conformations, the deviation of the $[\text{Fe}(\text{S}_2\text{-}o\text{-}xyl)_2]^{2-}$ from the $\omega \approx 0^\circ$ D_{2d} conformation is relatively minor, yielding a d_z^2 ground state like that predicted for $[\text{Fe}^{\text{II}}\{(\text{EPH}_2)_2\text{N}\}_2]$ for $\omega < 10^\circ$, see Figure 6, left.

An interesting feature of the potential energies presented in Figure 6, top, is that the predicted energies of the Fe^{II} and Zn^{II} analogues are very similar. This observation suggests that the geometries of the iron sites are determined not by electronic factors but rather by steric effects such as interligand electrostatic repulsions. This is unexpected when considering that unlike Zn^{II} sites which are Jahn–Teller (JT) inactive, high-spin Fe^{II} sites with a pseudo-tetrahedral symmetry have quasi-degenerate ground states (^5E) which are potentially JT active. However, a theoretical study of the JT effect in tetrathiolato complexes concluded that the experimentally observed distortions of reported FeS_4 cores are not the result of a (pseudo) JT effect.⁸⁸ This conclusion is consistent with our DFT calculations and suggests that for **1** and **2**, the relative orientation of the chalcogen-based lone pairs controls not only the electronic structure of the Fe^{II} sites but also their stereochemistry.

While the magnitude of the predicted quadrupole splitting is nearly ω -independent, for both $[\text{Fe}(\text{SMe})_4]^{2-}$ and $[\text{Fe}$

Table 3. DFT-Predicted efg Tensor Components, Expressing $eQV_{ii}/2$ in mm/s, and Isomer Shift Values Obtained for the Geometry-Optimized $[\text{Fe}\{(\text{EPMe}_2)_2\text{N}\}_2]$ Models of **1** and **2** at the B3LYP/6-311G Level of Theory^a

complex	contribution	efg tensor components				η	ΔE_Q (mm/s)	δ (mm/s)
		V_{xx}	V_{yy}	V_{zz}				
1	valence	-2.475	-1.280	3.755	0.318	3.818		
	ligand	-0.018	-0.086	0.104	0.656	0.111		
	total	-2.493	-1.366	3.859	0.292	3.913	0.677	
	experimental	-2.73	-0.68	3.42	0.6	3.62	0.82	
2	valence	-2.342	-1.392	3.735	0.254	3.775		
	ligand	0.015	-0.209	0.194	0.856	-0.233		
	total	-2.327	-1.602	3.929	0.185	3.951	0.613	
	experimental	-2.46	-1.05	3.52	0.4	3.61	0.78	

^aThe ligand contribution was estimated for models obtained by substituting Fe^{II} by Zn^{II} ions and using the same -1.6 mm/s/au conversion factor ($Q = 0.17$ b).

$\{(\text{EPH}_2)_2\text{N}\}_2$, see Figure S15, the rhombicity parameter η of the efg tensor is essentially linearly dependent on ω , see Figure 6, bottom.⁸⁹ Reflections such as those observed for $[\text{Fe}(\text{SMe})_4]^{2-}$ at $\omega \approx 11, 26,$ and 48° are due to the $|\eta| \leq 1$ convention and indicate a change in the relative magnitude of the $|V_z| \geq |V_x| \geq |V_y|$ efg tensor components. The overlay of the DFT-predicted η values on those derived from eq 8, for the valence-only contribution, see Figure S16, suggests that to a first approximation, $\theta \approx \omega + n\frac{\pi}{6}$. We note that despite this seemingly simple correspondence, the magnitude of the $\Delta\theta = 90^\circ$ interval for which the CF model described in the previous section predicts a dominant $d_{x^2-y^2}$ ground state is nearly three times larger than the interval derived from DFT ($\Delta\omega \approx 36^\circ$). This observation demonstrates that while our CF and DFT theoretical models are complementary, they are not equivalent. Despite being supported by different S/Se ligands, the quadrupole splitting of **1** is nearly identical to that of **2**. Although striking, this similarity is not unprecedented. Specifically, even though they have different symmetries, the ΔE_Q of $\text{Cp-Rd}_{\text{red}}$ is -3.24 mm/s, that of $[\text{Fe}(\text{SPH}_4)]^{2-}$ is -3.25 mm/s, and that for the Holm–Ibers complex, $[\text{Fe}(\text{S}_2\text{-o-oxyl})_2]^{2-}$ is -3.34 mm/s. For the latter compounds, their nearly identical ΔE_Q values arise from the efg tensor being independent of both θ and ω when only the valence contribution is considered in an S_4 distortion. This argument may be extended also to the D_2 distortion discussed above. The validity of the valence-only expressions is supported by inspection of Table 3 which shows that for both **1** and **2**, the DFT-predicted ligand contribution to the efg tensor (second row, ligand contribution) is an order of magnitude smaller than the valence contribution (first row, valence contribution). Therefore, the B3LYP/6-311G-predicted values of the efg parameters and of the isomer shift obtained for the geometry-optimized structures of the $[\text{Fe}\{(\text{EPMe}_2)_2\text{N}\}_2]$ models are in good agreement with the experiment. Table S9 shows that the prediction of a vanishing efg ligand contribution is a common feature of all DFT methods considered in this study, which is reproduced even when larger basis sets are employed. Increasing the basis set, changing the peripheral ligand groups and the symmetry of the model used, or using the experimental structures as the results summarized in Tables S7b, S8b, and S10b show lead to only a marginal improvement of the agreement between the theoretical and experimental values.

The Löwdin and Mulliken atomic and orbital charges and spin populations presented in Tables S10–S12 demonstrate that, as expected, regardless of the DFT method considered,

the predicted ground states of **1** and **2** have a $d_{x^2-y^2}$ character, and their electronic configuration are best described using the $|(\text{xy})^\alpha(\text{yz})^\alpha(\text{xz})^\alpha(\text{z}^2)^\alpha(\text{x}^2-\text{y}^2)^2|$ Slater determinant. The small ($\rho < 0.18$), spin-up density delocalized over the $(\text{EP})_2\text{N}$ ligand backbone is of the same sign as that localized on the central metal ion. This distribution of unpaired spin density is consistent with covalent bonding and redox-inactive (“innocent”) ligands. Just as implied by the similarity of their zero-field Mössbauer parameters, despite the different S/Se coordination environment, the DFT-predicted ground state electronic configurations of **1** and **2** are very similar.

4.3. Investigation of zfs in **1 and **2** Using Quantum Chemical Calculations.** Perhaps the most surprising observation derived from the spectroscopic investigation of **1** and **2** is that replacing the lighter S-containing ligands by their heavier Se-analogues leads to a smaller $|D|$ value, see Table 1. We anticipated that due to the greater relativistic effects induced by the heavier Se nuclei, the ligand SOC effect would be enhanced for the Se compound⁹⁰ and its magnetic anisotropy will be increased. This trend is sometimes referred to as the “heavy-atom effect”.^{91–93} However, many other factors may contribute to the overall zfs of metal complexes, including ligand-induced changes in the splitting of d orbitals, covalency, excitation energies, and the stabilization of metal-to-ligand charge transfer states.⁹⁴ Moreover, the influence of the ligand SOC is expected to be stronger for cases where the ligands are non-innocent, that is, when the ligands accommodate a large fraction of the total unpaired spin-density. However, the analysis of the DFT-predicted ground states coupled with the strong similarity of efg tensors suggests that the ligand contributions to the total zfs of both **1** and **2** are relatively modest and of similar magnitudes.

To delineate the factors responsible for the observed zfs values of **1** and **2**, we performed a series of CP DFT calculations on experimental, see Tables S7a and S8a, and geometry-optimized structures, see Table S10a. Unfortunately, these results are very poor. In contrast to the predicted ΔE_Q values, none of the methods considered (B3LYP, BP86, TPSSH /6-311G, 6-311+G*) yielded a satisfactory agreement between the experimental and theoretical D values, regardless of whether the experimental or optimized structures were used. For example, inspection of Table S7a shows that for the experimental unabridged structural models, B3LYP/6-311G predicted a positive and B3LYP/6-311+G* a negative D value for **1**, even though the corresponding computed E/D values are much lower than $1/3$ ($E/D \leq 0.127$). Although these methods yield a negative D value for **2**, in this case, its magnitude is

Table 4. Computed zfs Parameters and g Tensors Derived from CASSCF/NEVPT2(5,6) and CASSCF/NEVPT2(9,14) Calculations Performed on Truncated Models Derived from the Experimental Structures of Site a Considering Five Quintet and 10 Triplet States, $S = 2$ (5) $S = 1$ (10)

#	CAS	method	D	E/D	g_{min}	g_{mid}	g_{max}
1	5,6	CASSCF	-6.318	0.083	2.041	2.068	2.156
		NEVPT2	-5.491	0.055	2.034	2.053	2.125
	9,14	CASSCF	-6.241	0.092	2.039	2.067	2.154
		NEVPT2	-5.970	0.059	2.036	2.058	2.137
	experimental		-6.32	0.131	1.997	2.03	2.068
2	5,6	CASSCF	-5.833	0.194	2.038	2.086	2.160
		NEVPT2	-4.964	0.159	2.030	2.065	2.124
	9,14	CASSCF	-5.730	0.201	2.037	2.085	2.157
		NEVPT2	-5.386	0.167	2.033	2.072	2.136
	experimental		-4.53	0.194	2.054	2.097	2.19

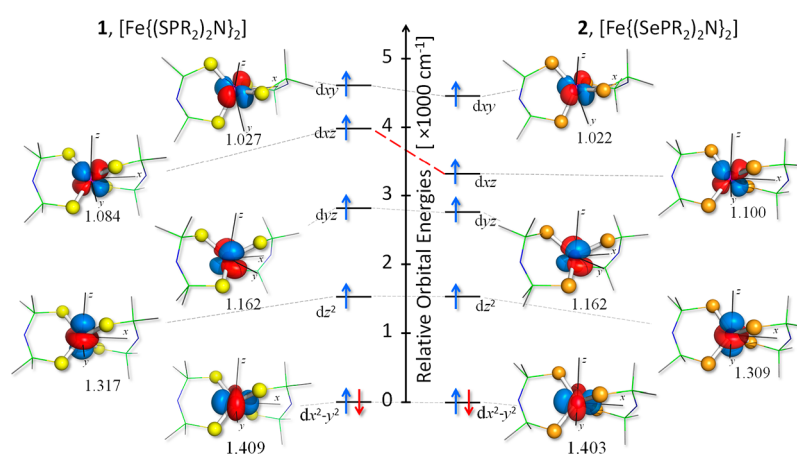


Figure 7. Crystal-field splitting diagram and ground state electronic configuration derived from the CASSCF(5,6) calculations performed for **1** (left) and **2** (right). The respective orbital populations of the active space orbitals comprising this figure are listed below each orbital. The coordinate system indicates the predicted orientation of the zfs tensor. The dashed red line highlights the ligand-dependent change of the d_{xz} orbital energy.

Table 5. CASSCF-Derived Transition Energies of $d-d$ Excitations (cm^{-1})

#	method	$d_{x^2-y^2}^\beta \rightarrow d_{z^2}^\beta$	$d_{x^2-y^2}^\beta \rightarrow d_{yz}^\beta$	$d_{x^2-y^2}^\beta \rightarrow d_{xz}^\beta$	$d_{x^2-y^2}^\beta \rightarrow d_{xy}^\beta$
1	CASSCF(5,6) ^a	1524	2809	3973	4612
	CASSCF/NEVPT2(5,6) ^a	2073	3418	5056	5803
	AILFT CASSCF(5,6) ^{b,c,d}	1377	2813	3856	4390
	experimental ^e	$\geq 600^f$		4300 ^g	
2	CASSCF(5,6) ^a	1524	2758	3316	4447
	CASSCF/NEVPT2(5,6) ^a	2119	3499	4372	5788
	AILFT CASSCF(5,6) ^{b,c,h}	1393	2794	3228	4252
	experimental ^e	$\geq 600^f$	2570	1960	3910

^aValues obtained considering 5 quintet and 10 triplet states. ^bValues obtained considering 5 quintet and 35 triplet states. ^cTransition energies derived from the ligand field splitting of one-electron eigenfunctions. ^dThe ground state coefficients of the d_{z^2} and $d_{x^2-y^2}$ contributions are $\alpha = 0.119548$ $\beta = 0.991553$. While this β value suggests that $\theta_{th} = 82.5^\circ$, the experimental value of this mixing parameter is $\theta_{exp} = 83.5^\circ$. ^eValues derived from the CF analysis of the sH parameters presented in section 4.1. ^fValues determined from the temperature dependence of the ΔE_Q values, $\Delta E_Q(T) = \Delta E_Q(4.2K) \tanh(2\epsilon kT)$. ^gvalue obtained imposing $\epsilon(d_{xz}) = \epsilon(d_{yz}) = \epsilon(d_{xy}) = \epsilon(t_2)$. ^hThe ground state coefficients of the d_{z^2} and $d_{x^2-y^2}$ contributions are $\alpha = 0.148346$ and $\beta = 0.988767$. Coincidentally, these values lead to a mixing parameter $\theta_{th} = 83.6^\circ$, which compares very well with the $\theta_{exp} = 83.6^\circ$ experimental value.

nearly 10 times larger than the experimental value. Inspection of the individual contributions to D , listed in Table S14a,b, shows that for both **1** and **2**, D is dominated by the SOC interaction and that the contribution of the SSC interactions is relatively small, $|D_{SSC}| \leq 0.45$ cm^{-1} . We note that the latter value compares quite well with that derived from the CF analysis of the sH parameters, $D_{SSC} \cong -0.53$ cm^{-1} . In general, the contribution of spin-conserving excitations, $\alpha \rightarrow \alpha$ and

$\beta \rightarrow \beta$, are dominant with the quintet states, $\beta \rightarrow \beta$ providing the largest component. The dominant triplet excited state contribution to D originates from $\alpha \rightarrow \beta$ spin-flip excitations. A poor performance of CP DFT has been also noted by Maganas et al. in calculating the zfs of $Co^{II}S_4$ -containing complexes.⁹⁵ Therefore, our work reinforces their conclusion that this methodology has a limited applicability for this class of $[M^{II}E_4]$ compounds (where $M = Fe, Co$).

Inspection of Table 4 and Table S18 shows that unlike CP DFT, our CASSCF and CASSCF/NEVPT2 calculations perform very well in reproducing both the sign and the magnitude of D in **1** and **2**. To quantify the influence of the ligand SOC, we have considered two distinct active spaces, namely, CAS(5,6), which spans the canonical 3d orbitals of the Fe^{II} ions and includes six electrons, see Figure 7, and the CAS(9,14) active space obtained by expanding the CAS(5,6) to incorporate one lone-pair of electrons localized on each of the four S/Se atoms, see Figure S17. The expansion of the active space had a marginal effect on the predicted zfs values, again suggesting that the SOC of the S/Se ligands does not play a direct role in determining the magnetic anisotropy of these compounds. This observation is consistent with the expected ionic character of the CASSCF wavefunctions and suggests that a different factor must be responsible for the difference between the zfs values of **1** and **2**.

The difference between the experimental D values of **1** and **2** is 1.82 cm^{-1} corresponding to a 28% decrease in the magnitude of $D(1)$. Although the theoretical CASSCF and CASSCF/NEVPT2 values reproduce this trend, the computational reduction is smaller than that observed experimentally, ranging from 5 to 11% of the predicted $D(1)$, that is, a difference of $0.29\text{--}0.63 \text{ cm}^{-1}$. The theoretical values listed in Table S18 allow us to distinguish two trends: (i) the quintets' contribution to the zfs is $\sim 0.3\text{--}0.4 \text{ cm}^{-1}$ smaller for **2** than that for **1** and (ii) the triplets' contribution is also $\sim 0.2 \text{ cm}^{-1}$ smaller for **2** than that for **1**.

Comparing the excitation energies of the d–d excitations, which are listed in Table 5 and Table S14a,b, reveals that regardless of the theoretical method used, the energy of the $d_{x^2-y^2}^{\beta} \rightarrow d_{xz}^{\beta}$ transition of **1** is nearly always $\sim 600 \text{ cm}^{-1}$ larger than that of **2**. Inspection of eq 11, which lists the perturbation theory expression of the quintets' contribution to D for a $d_{x^2-y^2}$ ground state, shows that this transition energy may indeed be responsible for the lower magnitude of $D_{S=2}$ of **2**. Unfortunately, no analogous factor could be identified to account for the systematic difference in the excited triplet states' contribution to D , $D_{S=1}$.

$$D_{S=2} = -\frac{4\lambda^2}{\varepsilon(d_{xy})} + \frac{\lambda^2}{\varepsilon(d_{xz})} + \frac{\lambda^2}{\varepsilon(d_{yz})} \quad (11)$$

The composition of the orbitals spanning the active spaces of the CASSCF(5,6) and CASSCF(9,14) is listed in Table S15. The metal-based orbitals of the CAS(5,6) active space are presented in Figure 7 and the ligand-based orbitals of the CAS(9,14) are shown in Figure S17. As with the DFT-predicted ground state, the CASSCF/NEVPT2-derived ground states have a $d_{x^2-y^2}$ character, see Tables S15 and S16. The decomposition of the predicted zfs tensors, see Table S17a,b, shows that, just as expected, the large $\langle d_{x^2-y^2} | \hat{L}_z | d_{xy} \rangle = -2i$ matrix element gives the $d_{x^2-y^2}^{\beta} \rightarrow d_{xy}^{\beta}$ excitation the largest contribution to the zfs values of **1** and **2** even though d_{xy} has the highest orbital energy. Although the contributions of the $d_{x^2-y^2}^{\beta} \rightarrow \{d_{yz}^{\beta}, d_{xz}^{\beta}\}$ transitions have an opposite sign (positive, as opposed to negative for the $d_{x^2-y^2}^{\beta} \rightarrow d_{xy}^{\beta}$ excitation), consistent with eq 11, they are considerably smaller, which leads to an overall negative zfs. The predicted contribution of the excited triplet states to the zfs values of **1** range, depending on the composition of the active space and the number of states considered, from -0.14 to -1.38 cm^{-1} , which is

comparable with the $D_{S=1} = -1.22 \text{ cm}^{-1}$ value derived from the analysis of the sH parameters.

To evaluate the effect of a D_2 distortion on the predicted efg and zfs of **1** and **2**, we performed a series of CASSCF(5,6) calculations on geometry-optimized D_2/D_{2d} structural models obtained using DFT at the B3LYP/6-311G level of theory, see Figure 8. These calculations indicate that the character of the ground state and the rhombicity of the efg and D tensors are exquisitely dependent on the magnitude of the D_2 distortion.

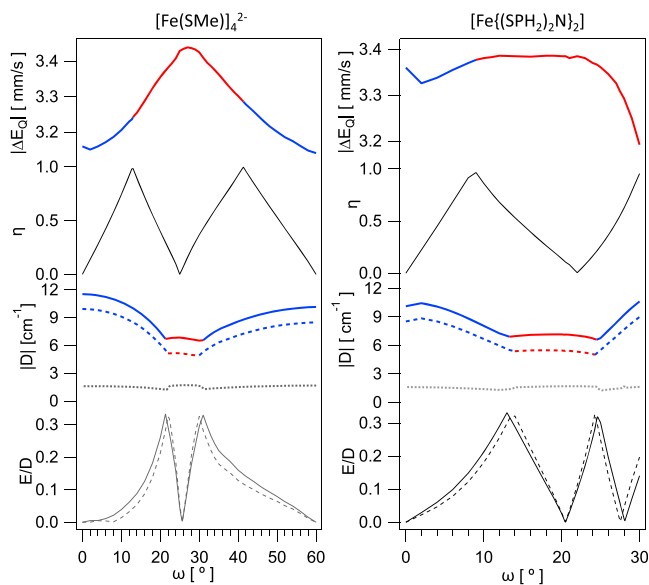


Figure 8. CASSCF(5,6)-predicted effects of a D_2 distortion on the efg (top) and zfs (bottom) parameters of $[\text{Fe}(\text{SMe})_4]^{2-}$ (left) and $[\text{Fe}\{(\text{SPH}_2)_2\text{N}\}_2]$ (right). The positive ΔE_Q and D values are shown in red, and the corresponding negative values are shown in blue. The D and E/D traces obtained when all 5 quintet and 35 triplet states were included in the CASSCF calculations are shown using a solid line; those obtained when only the five quintets were considered are shown using a dashed line; and the contribution of the triplet states, obtained by taking the difference between the previous two, is shown using a dotted line.

Overall, the CASSCF(5,6)-predicted efg tensors reproduced the $\eta(\omega)$ derived from the DFT calculations. Therefore, the distortion along ω induces a switch in the sign of both ΔE_Q and D values, consistent with a change in the nature of the ground state. However, the range of ω values for which these values are positive are not congruent. This pattern is reminiscent of the crystal-field predicted behavior for the case where the energies of the t_2 orbitals are unequal, see Figure S12. Finally, while the CASSCF-predicted η shows a linear dependence on ω , the correlation of the E/D values with this structural parameter is more complicated, given that a quasi-quadratic dependence is observed at low ω values.

5. CONCLUSIONS

We describe the electronic structure of two high-spin $S = 2$ complexes, **1** and **2**, which enclose tetrahedral Fe^{II}E₄ cores (E = S, Se). These compounds were investigated using advanced spectroscopic methods including HFEP and field-dependent Mössbauer spectroscopy, which afforded accurate sH parameters including D , E/D , g values, as well as ⁵⁷Fe electric field gradients and hyperfine coupling tensors. These parameters were rationalized by computational studies, which employed

both DFT and *ab initio* CASSCF methods. These studies revealed that the ligand-based SOC plays an insignificant role in setting the *zfs* of these complexes and that instead, the difference between the magnetic anisotropy of **1** and **2** may be traced to different d–d excitation energies. Finally, the electronic structure of these compounds could be corroborated very well with that of other Fe^{II}S₄ analogues, including Rd_{red}, by considering a structural distortion along a D₂-symmetric coordinate.

■ ASSOCIATED CONTENT

Supporting Information

The Supporting Information is available free of charge at <https://pubs.acs.org/doi/10.1021/acs.inorgchem.1c00670>.

Literature review, summary of crystallographic data, and additional HFEP, Mössbauer, and computational data (PDF)

■ AUTHOR INFORMATION

Corresponding Authors

Sebastian A. Stoian – Department of Chemistry, University of Idaho, Moscow, Idaho 83844, United States; orcid.org/0000-0003-3362-7697; Email: sstoian@uidaho.edu

Panayotis Kyritsis – Inorganic Chemistry Laboratory, Department of Chemistry, National and Kapodistrian University of Athens, 15771 Athens, Greece; orcid.org/0000-0002-3908-4649; Email: kyritsis@chem.uoa.gr

Authors

Mahsa Moshari – Department of Chemistry, University of Idaho, Moscow, Idaho 83844, United States

Eleftherios Ferentinos – Inorganic Chemistry Laboratory, Department of Chemistry, National and Kapodistrian University of Athens, 15771 Athens, Greece

Alexios Grigoropoulos – Inorganic Chemistry Laboratory, Department of Chemistry, National and Kapodistrian University of Athens, 15771 Athens, Greece

J. Krzystek – National High Magnetic Field Laboratory, Florida State University, Tallahassee, Florida 32310, United States; orcid.org/0000-0001-6088-1936

Joshua Telser – Department of Biological, Physical, and Health Sciences, Roosevelt University, Chicago, Illinois 60605, United States; orcid.org/0000-0003-3307-2556

Complete contact information is available at: <https://pubs.acs.org/doi/10.1021/acs.inorgchem.1c00670>

Notes

The authors declare no competing financial interest.

■ ACKNOWLEDGMENTS

This work was supported in part by the University of Idaho (S.A.S) and the Special Research Account of the National and Kapodistrian University of Athens (P.K.). M.M. acknowledges the support of the Donald & Velsie Snyder Chemistry Scholarship. We thank Dr. Andrew Ozarowski for his EPR simulation and fitting program SPIN, as well as for helpful discussions. Part of this work was performed at the National High Magnetic Field Laboratory (NHMFL), funded by National Science Foundation through Cooperative Agreement DMR 1157490 and 1644779 and the State of Florida. The Fulbright Foundation in Greece and the NHMFL via its Visiting Scientist Program supported a scientific extended visit

of P.K. to the latter. P.K. would like to dedicate this article to Dr. Jean-Marc Moulis, his mentor in Fe/S chemistry, on the occasion of his retirement. We would like to thank all Reviewers for their constructive comments.

■ REFERENCES

- (1) Holm, R. H.; Kennepohl, P.; Solomon, E. I. Structural and Functional Aspects of Metal Sites in Biology. *Chem. Rev.* **1996**, *96*, 2239–2314.
- (2) Solomon, E. I.; Gorelsky, S. I.; Dey, A. Metal-thiolate bonds in bioinorganic chemistry. *J. Comput. Chem.* **2006**, *27*, 1415–1428.
- (3) Beinert, H.; Holm, R. H.; Münck, E. Iron-sulfur clusters: nature's modular, multipurpose structures. *Science* **1997**, *277*, 653–659.
- (4) Meyer, J.; Moulis, J.-M. Rubredoxin. In *Handbook of Metalloproteins*; Messerschmidt, A.; Huber, R.; Poulos, T.; Wieghardt, K.; Eds.; John Wiley & Sons: 2006, DOI: [10.1002/0470028637.met135](https://doi.org/10.1002/0470028637.met135).
- (5) Coelho, A. V.; Matias, P.; Fülöp, V.; Thompson, A.; Gonzalez, A.; Carrondo, M. A. Desulfoferrodoxin structure determined by MAD phasing and refinement to 1.9-Å resolution reveals a unique combination of a tetrahedral FeS₄ centre with a square pyramidal FeSN₄ centre. *J. Biol. Inorg. Chem.* **1997**, *2*, 680–689.
- (6) Goodfellow, B. J.; Moura, J. J. G.; Rusnak, F.; Domke, T. NMR determination of the global structure of the ¹¹³Cd derivative of desulfoferrodoxin: Investigation of the hydrogen bonding pattern at the metal center. *Protein Sci.* **1998**, *7*, 928–937.
- (7) Coucouvanis, D.; Swenson, D.; Baenziger, N. C.; Holah, D. G.; Kostikas, A.; Simopoulos, A.; Petrouleas, V. Crystal and molecular structures of [(C₆H₅)₄P]₂Fe(S₂C₄O₂)₂ and [(C₆H₅)₄P]₂Fe(SC₆H₅)₄, a structural analog of reduced rubredoxin. *J. Am. Chem. Soc.* **1976**, *98*, 5721–5723.
- (8) Coucouvanis, D.; Swenson, D.; Baenziger, N. C.; Murphy, C.; Holah, D. G.; Sfarnas, N.; Simopoulos, A.; Kostikas, A. Tetrahedral complexes containing the Fe(II)S₄ core. The syntheses, ground-state electronic structures and crystal and molecular structures of the bis(tetraphenylphosphonium) tetrakis (thiophenolato)ferrate (II) and bis (tetraphenyl phosphonium) bis(dithiosquarato)ferrate (II) complexes. An analog for the active site in reduced rubredoxin (Rdred). *J. Am. Chem. Soc.* **1981**, *103*, 3350–3362.
- (9) Gebhard, M. S.; Koch, S. A.; Millar, M.; Devlin, F. J.; Stephens, P. J.; Solomon, E. I. Single-crystal spectroscopic studies of Fe(SR)₄²⁻ (R = 2-(Ph)C₆H₄): electronic structure of the ferrous site in rubredoxin. *J. Am. Chem. Soc.* **1991**, *113*, 1640–1649.
- (10) Ueyama, N.; Okamura, T. A.; Nakamura, A. Intramolecular NH...S hydrogen-bond in *o*-acylamino substituted benzenethiolate iron(II) and cobalt(II) complexes. *J. Chem. Soc., Chem. Commun.* **1992**, 1019–1020.
- (11) Silver, A.; Koch, S. A.; Millar, M. X-ray crystal-structures of a series of [M^{II}(SR)₄]²⁻ complexes (M = Mn, Fe, Co, Ni, Zn, Cd and Hg) with S₄ crystallographic symmetry. *Inorg. Chim. Acta* **1993**, *205*, 9–14.
- (12) Okamura, T.-A.; Takamizawa, S.; Ueyama, N.; Nakamura, A. Novel Rubredoxin Model Tetrathiolato Iron(II) and Cobalt(II) Complexes Containing Intramolecular Single and Double NH...S Hydrogen Bonds. *Inorg. Chem.* **1998**, *37*, 18–28.
- (13) Bose, K.; Huang, J.; Haggerty, B. S.; Rheingold, A. L.; Salm, R. J.; Walters, M. A. Evidence for Charge-Dipole Effects in the Rubredoxin Model Compound [(CH₃)₄N]₂Fe[SCH₂CON(CH₃)₂]₄. *Inorg. Chem.* **1997**, *36*, 4596–4599.
- (14) Lane, R. W.; Ibers, J. A.; Frankel, R. B.; Papaefthymiou, G. C.; Holm, R. H. Synthetic analogs of the active sites of iron-sulfur proteins. 14. Synthesis, properties, and structures of bis(*o*-xylyl- α,α' -dithiolato)ferrate(II,III) anions, analogs of oxidized and reduced rubredoxin sites. *J. Am. Chem. Soc.* **1977**, *99*, 84–98.
- (15) Chung, W. P.; Dewan, J. C.; Tuckerman, M.; Walters, M. A. Effect of N-H...S amide-thiolate hydrogen bonding on bond lengths in rubredoxin models [(CH₃)₃NCH₂CONH]₂[M(S₂-*o*-xyl)₂]. *Inorg. Chim. Acta* **1999**, *291*, 388–394.

- (16) McConnachie, J. M.; Ibers, J. A. Synthesis of the PPh_4^+ and NET_4^+ Salts of $\text{M}(\text{SePh})_4^{2-}$ ($\text{M} = \text{Mn, Fe, Co, Ni}$) and the Structure of $[\text{NET}_4]_2[\text{Fe}(\text{SePh})_4] \cdot \text{MeCN}$. *Inorg. Chem.* **1991**, *30*, 1770–1773.
- (17) Eichhöfer, A.; Buth, G.; Dolci, F.; Fink, K.; Mole, R. A.; Wood, P. T. Homoleptic 1-D iron selenolate complexes-synthesis, structure, magnetic and thermal behaviour of $[\text{Fe}(\text{SeR})_2]$ ($\text{R} = \text{Ph, Mes}$). *Dalton Trans.* **2011**, *40*, 7022–7032.
- (18) Flörke, U.; Hammann, B.; Henkel, G. *Cambridge Structural Database Communication*; 2016.
- (19) Kim, K. W.; Kim, J. Crystal structure of bis-(tetraphenylphosphonium)-bis(1,4-tetraselenido- $\kappa^2\text{Se}^1, \text{Se}^4$)ferrite(II), $\text{C}_{48}\text{H}_{40}\text{FeP}_2\text{Se}_8$. *Z. Kristallogr. - New Cryst. Struct.* **2014**, *229*, 31–34.
- (20) Akhtar, M.; Malik, M. A.; Raftery, J.; O'Brien, P. Synthesis of iron selenide nanocrystals and thin films from bis-(tetraisopropylidisenoidodiphosphinato)iron(II) and bis-(tetraphenyldisenoidodiphosphinato)iron(II) complexes. *J. Mater. Chem. A* **2014**, *2*, 20612–20620.
- (21) Pugh, T.; Layfield, R. A. Reactivity of three-coordinate iron-NHC complexes towards phenylselenol and lithium phenylselenide. *Dalton Trans.* **2014**, *43*, 4251–4254.
- (22) Stadelman, B. S.; Kimani, M. M.; Bayse, C. A.; McMillen, C. D.; Brumaghim, J. L. Synthesis, characterization, DFT calculations, and electrochemical comparison of novel iron(II) complexes with thione and selenone ligands. *Dalton Trans.* **2016**, *45*, 4697–4711.
- (23) Ferentinos, E.; Chatziefthimiou, S.; Boudalis, A. K.; Pissas, M.; Mathies, G.; Gast, P.; Groenen, E. J. J.; Sanakis, Y.; Kyritsis, P. The $[\text{Fe}\{(\text{SePPh}_2)_2\text{N}\}_2]$ Complex Revisited: X-ray Crystallography, Magnetometry, High-Frequency EPR, and Mössbauer Studies Reveal Its Tetrahedral $\text{Fe}^{\text{II}}\text{Se}_4$ Coordination Sphere. *Eur. J. Inorg. Chem.* **2018**, *713*–721.
- (24) Silvestru, C.; Drake, J. E. Tetraorganodichalcogenoidodiphosphorus acids and their main group metal derivatives. *Coord. Chem. Rev.* **2001**, *223*, 117–216.
- (25) Ly, T. Q.; Woollins, J. D. Bidentate organophosphorus ligands formed via P-N bond formation: synthesis and coordination chemistry. *Coord. Chem. Rev.* **1998**, *176*, 451–481.
- (26) Haiduc, I. Dichalcogenoidodiphosphinato Ligands. In *Comprehensive Coordination Chemistry II: From Biology to Nanotechnology*; McCleverty, J. A., Meyer, T. J., Eds.; Elsevier: Amsterdam, The Netherlands, 2004; Vol. 1, pp. 323–347.
- (27) Churchill, M. R.; Wormald, J. Crystal structure of bis-(imidotetramethyldithiodiphosphino-S,S)iron(II), a complex with tetrahedral iron tetrasulfide core. *Inorg. Chem.* **1971**, *10*, 1778–1782.
- (28) Davison, A.; Switkes, E. S. Stereochemistry of four-coordinate bis(imidodiphosphinato)metal(II) chelate complexes. *Inorg. Chem.* **1971**, *10*, 837–842.
- (29) Czernuszewicz, R.; Maslowsky, E., Jr.; Nakamoto, K. Infrared and raman spectra of bis(imidotetraphenyldithiodiphosphino-S,S') complexes with Cu(II), Co(II) and Fe(II)d. *Inorg. Chim. Acta* **1980**, *40*, 199–202.
- (30) Siiman, O.; Vetuskey, J. Synthesis of copper thio- and dithioimidodiphosphinates. Infrared and Raman spectra of imidodiphosphinates. *Inorg. Chem.* **1980**, *19*, 1672–1680.
- (31) Mathies, G.; Chatziefthimiou, S. D.; Maganas, D.; Sanakis, Y.; Sottini, S.; Kyritsis, P.; Groenen, E. J. J. High-frequency EPR study of the high-spin Fe^{II} complex $[\text{Fe}\{(\text{SPPH}_2)_2\text{N}\}_2]$. *J. Magn. Reson.* **2012**, *224*, 94–100.
- (32) Levesanos, N.; Liyanage, W. P. R.; Ferentinos, E.; Raptopoulos, G.; Paraskevopoulou, P.; Sanakis, Y.; Choudhury, A.; Stavropoulos, P.; Nath, M.; Kyritsis, P. Investigating the Structural, Spectroscopic, and Electrochemical Properties of $[\text{Fe}\{(\text{EP}^i\text{Pr}_2)_2\text{N}\}_2]$ ($\text{E} = \text{S, Se}$) and the Formation of Iron Selenides by Chemical Vapor Deposition. *Eur. J. Inorg. Chem.* **2016**, *5332*–5339.
- (33) Hagen, W. R. EPR of non-Kramers doublets in biological systems: Characterization of an $S = 2$ system in oxidized cytochrome c oxidase. *Biochim. Biophys. Acta, Protein Struct. Mol. Enzymol.* **1982**, *708*, 82–98.
- (34) Hendrich, M. P.; Debrunner, P. G. EPR Spectra of Quintet Ferrous Myoglobin and a Model Heme Compound. *J. Magn. Reson.* **1988**, *78*, 133–141.
- (35) Hendrich, M. P.; Debrunner, P. G. Integer-Spin Electron-Paramagnetic Resonance of Iron Proteins. *Biophys. J.* **1989**, *56*, 489–506.
- (36) Hu, C.; Sulok, C. D.; Paulat, F.; Lehnert, N.; Twigg, A. I.; Hendrich, M. P.; Schulz, C. E.; Scheidt, W. R. Just a Proton: Distinguishing the Two Electronic States of Five-Coordinate High-Spin Iron(II) Porphyrinates with Imidazole/ate Coordination. *J. Am. Chem. Soc.* **2010**, *132*, 3737–3750.
- (37) Werth, M. T.; Kurtz, D. M., Jr.; Howes, B. D.; Huynh, B. H. Observation of $S = 2$ EPR Signals from Ferrous Iron Thiolate Complexes - Relevance to Rubredoxin-Type Sites in Proteins. *Inorg. Chem.* **1989**, *28*, 1357–1361.
- (38) Krzystek, J.; Ozarowski, A.; Telsler, J. Multi-frequency, high-field EPR as a powerful tool to accurately determine zero-field splitting in high-spin transition metal coordination complexes. *Coord. Chem. Rev.* **2006**, *250*, 2308–2324.
- (39) Telsler, J.; Ozarowski, A.; Krzystek, J. High-frequency and -field electron paramagnetic resonance of transition metal ion (d block) coordination complexes. *Electron Paramagn. Reson.* **2012**, *23*, 209–263.
- (40) Krzystek, J.; Telsler, J. Measuring giant anisotropy in paramagnetic transition metal complexes with relevance to single-ion magnetism. *Dalton Trans.* **2016**, *45*, 16751–16763.
- (41) Andersson, K. K.; Schmidt, P. P.; Katterle, B.; Strand, K. R.; Palmer, A. E.; Lee, S.-K.; Solomon, E. I.; Gräslund, A.; Barra, A.-L. Examples of high-frequency EPR studies in bioinorganic chemistry. *J. Biol. Inorg. Chem.* **2003**, *8*, 235–247.
- (42) Telsler, J.; Krzystek, J.; Ozarowski, A. High-frequency and high-field electron paramagnetic resonance (HF-EPR): a new spectroscopic tool for bioinorganic chemistry. *J. Biol. Inorg. Chem.* **2014**, *19*, 297–318.
- (43) Knapp, M. J.; Krzystek, J.; Brunel, L.-C.; Hendrickson, D. N. High-Frequency EPR Study of the Ferrous Ion in the Reduced Rubredoxin Model $[\text{Fe}(\text{SPh})_4]^{2-}$. *Inorg. Chem.* **2000**, *39*, 281–288.
- (44) Barra, A. L.; Hassan, A. K.; Janoschka, A.; Schmidt, C. L.; Schünemann, V. Broad-band quasi-optical HF-EPR spectroscopy: application to the study of the ferrous iron center from a rubredoxin mutant. *Appl. Magn. Reson.* **2006**, *30*, 385–397.
- (45) Zadrozny, J. M.; Greer, S. M.; Hill, S.; Freedman, D. E. A flexible iron(II) complex in which zero-field splitting is resistant to structural variation. *Chem. Sci.* **2016**, *7*, 416–423.
- (46) Harman, W. H.; Harris, T. D.; Freedman, D. E.; Fong, H.; Chang, A.; Rinehart, J. D.; Ozarowski, A.; Sougrati, M. T.; Grandjean, F.; Long, G. J.; Long, J. R.; Chang, C. J. Slow Magnetic Relaxation in a Family of Trigonal Pyramidal Iron(II) Pyrrolide Complexes. *J. Am. Chem. Soc.* **2010**, *132*, 18115–18126.
- (47) Kostikas, A.; Petrouleas, V.; Simopoulos, A.; Coucouvanis, D.; Holah, D. G. Mössbauer-Effect in Synthetic Analogs of Rubredoxin. *Chem. Phys. Lett.* **1976**, *38*, 582–584.
- (48) Winkler, H.; Bill, E.; Trautwein, A. X.; Kostikas, A.; Simopoulos, A.; Terzis, A. Static and Dynamic Hyperfine Coupling of Fe(II) in the FeS_4 Unit - Results of Mössbauer-Spectroscopy on a $[\text{P}(\text{C}_6\text{H}_5)_4]_2[\text{Fe}(\text{SC}_6\text{H}_5)_4]$ Monocrystal. *J. Chem. Phys.* **1988**, *89*, 732–740.
- (49) Rao, K. K.; Evans, M. C. W.; Cammack, R.; Hall, D. O.; Thompson, C. L.; Jackson, P. J.; Johnson, C. E. Mössbauer effect in rubredoxin. Determination of the hyperfine field of the iron in a simple iron-sulphur protein. *Biochem. J.* **1972**, *129*, 1063–1070.
- (50) Schulz, C.; Debrunner, P. G. Rubredoxin, a simple iron-sulfur protein: its spin Hamiltonian and hyperfine parameters. *J. Phys. Colloques* **1976**, *153*–158.
- (51) Winkler, H.; Schulz, C.; Debrunner, P. G. Spin Fluctuation Rates from Mössbauer-Spectra of High-Spin Ferrous Rubredoxin. *Phys. Lett. A* **1979**, *69*, 360–363.
- (52) Yoo, S. J.; Meyer, J.; Achim, C.; Peterson, J.; Hendrich, M. P.; Münck, E. Mössbauer, EPR, and MCD studies of the C9S and C42S

variants of *Clostridium pasteurianum* rubredoxin and MCD studies of the wild-type protein. *J. Biol. Inorg. Chem.* **2000**, *5*, 475–487.

(53) Vrajmasu, V. V.; Bominaar, E. L.; Meyer, J.; Münck, E. Mössbauer study of reduced rubredoxin as purified and in whole cells. Structural correlation analysis of spin Hamiltonian parameters. *Inorg. Chem.* **2002**, *41*, 6358–6371.

(54) Jiang, S.-D.; Maganas, D.; Levesanos, N.; Ferentinos, E.; Haas, S.; Thirunavukkuarasu, K.; Krzystek, J.; Dressel, M.; Bogani, L.; Neese, F.; Kyritsis, P. Direct Observation of Very Large Zero-Field Splitting in a Tetrahedral Ni^{II}Se₄ Coordination Complex. *J. Am. Chem. Soc.* **2015**, *137*, 12923–12928.

(55) Sarkar, A.; Tewary, S.; Sinkar, S.; Rajaraman, G. Magnetic Anisotropy in (Co^{II}X₄) (X=O, S, Se) Single-Ion Magnets: Role of Structural Distortions versus Heavy Atom Effect. *Chem. – Asian J.* **2019**, *14*, 4696–4704.

(56) Mathonière, C.; Lin, H.-J.; Siretanu, D.; Clérac, R.; Smith, J. M. Photoinduced Single-Molecule Magnet Properties in a Four-Coordinate Iron(II) Spin Crossover Complex. *J. Am. Chem. Soc.* **2013**, *135*, 19083–19086.

(57) Werncke, C. G.; Bouammali, M.-A.; Baumard, J.; Suaud, N.; Martins, C.; Guihéry, N.; Vendier, L.; Zheng, J.; Sortais, J.-B.; Darcel, C.; Sabo-Etienne, S.; Sutter, J.-P.; Bontemps, S.; Pichon, C. Ising-type Magnetic Anisotropy and Slow Relaxation of the Magnetization in Four-Coordinate Amido-Pyridine Fe^{II} Complexes. *Inorg. Chem.* **2016**, *55*, 10968–10977.

(58) Sarkar, A.; Velmurugan, G.; Rajeshkumar, T.; Rajaraman, G. Deciphering the origin of invariance in magnetic anisotropy in {Fe^{II}S₄} complexes: a theoretical perspective. *Dalton Trans.* **2018**, *47*, 9980–9984.

(59) Hassan, A. K.; Pardi, L. A.; Krzystek, J.; Sienkiewicz, A.; Goy, P.; Rohrer, M.; Brunel, L.-C. Ultrawide band multifrequency high-field EMR technique: A methodology for increasing spectroscopic information. *J. Magn. Reson.* **2000**, *142*, 300–312.

(60) Münick, E.; Groves, J. L.; Tumolillo, T. A.; Debrunner, P. G. Computer simulations of Mössbauer spectra for an effective spin S=12 Hamiltonian. *Comput. Phys. Commun.* **1973**, *5*, 225–238.

(61) (a) Neese, F. The ORCA program system. *Wiley Interdiscip. Rev.: Comput. Mol. Sci.* **2012**, *2*, 73–78. (b) Neese, F. Software update: the ORCA program system, version 4.0. *Science* **2018**, *8*, e1327.

(62) Frisch, M. J.; Trucks, G. W.; Schlegel, H. B.; Scuseria, G. E.; Robb, M. A.; Cheeseman, J. R.; Scalmani, G.; Barone, V.; Mennucci, B.; Petersson, G. A.; Nakatsuji, H.; Caricato, M.; Li, X.; Hratchian, H. P.; Izmaylov, A. F.; Bloino, J.; Zheng, G.; Sonnenberg, J. L.; Hada, M.; Ehara, M.; Toyota, K.; Fukuda, R.; Hasegawa, J.; Ishida, M.; Nakajima, T.; Honda, Y.; Kitao, O.; Nakai, H.; Vreven, T.; Montgomery, J. A., Jr.; Peralta, J. E.; Ogliaro, F.; Bearpark, M.; Heyd, J. J.; Brothers, E.; Kudin, K. N.; Staroverov, V. N.; Kobayashi, R.; Normand, J.; Raghavachari, K.; Rendell, A.; Burant, J. C.; Iyengar, S. S.; Tomasi, J.; Cossi, M.; Rega, N.; Millam, J. M.; Klene, M.; Knox, J. E.; Cross, J. B.; Bakken, V.; Adamo, C.; Jaramillo, J.; Gomperts, R.; Stratmann, R. E.; Yazyev, O.; Austin, A. J.; Cammi, R.; Pomelli, C.; Ochterski, J. W.; Martin, R. L.; Morokuma, K.; Zakrzewski, V. G.; Voth, G. A.; Salvador, P.; Dannenberg, J. J.; Dapprich, S.; Daniels, A. D.; Farkas, O.; Foresman, J. B.; Ortiz, J. V.; Cioslowski, J.; Fox, D. J. *Gaussian. 2009 Gaussian, Inc.: Wallingford CT, 2009.*

(63) Perdew, J. P. Density-functional approximation for the correlation energy of the inhomogeneous electron gas. *Phys. Rev. B* **1986**, *33*, 8822–8824.

(64) Becke, A. D. Density-functional exchange-energy approximation with correct asymptotic behavior. *Phys. Rev. A* **1988**, *38*, 3098–3100.

(65) Jensen, K. P. Bioinorganic Chemistry Modeled with the TPSSH Density Functional. *Inorg. Chem.* **2008**, *47*, 10357–10365.

(66) Krishnan, R.; Binkley, J. S.; Seeger, R.; Pople, J. A. Self-consistent molecular orbital methods. XX. A basis set for correlated wave functions. *J. Chem. Phys.* **1980**, *72*, 650–654.

(67) Clark, T.; Chandrasekhar, J.; Spitznagel, G. W.; Schleyer, P. V. R. Efficient diffuse function-augmented basis sets for anion

calculations. III. The 3-21+G basis set for first-row elements, Li–F. *J. Comput. Chem.* **1983**, *4*, 294–301.

(68) Davidson, E. R.; Feller, D. Basis set selection for molecular calculations. *Chem. Rev.* **1986**, *86*, 681–696.

(69) Neese, F. Calculation of the zero-field splitting tensor on the basis of hybrid density functional and Hartree-Fock theory. *J. Chem. Phys.* **2007**, *127*, 164112.

(70) Bachrach, S. M. Population Analysis and Electron Densities from Quantum Mechanics. In *Rev. Comput. Chem. Vol V*; Lipkowitz, K. B.; Boyd, D. B. Eds.; VCH Publishers, Inc.: New York, 1994; pp. 171–228.

(71) Angeli, C.; Borini, S.; Cestari, M.; Cimraglia, R. A quasidegenerate formulation of the second order n-electron valence state perturbation theory approach. *J. Chem. Phys.* **2004**, *121*, 4043–4049.

(72) Angeli, C.; Cimraglia, R.; Evangelisti, S.; Leininger, T.; Malrieu, J.-P. Introduction of n-electron valence states for multi-reference perturbation theory. *J. Chem. Phys.* **2001**, *114*, 10252–10264.

(73) Weigend, F.; Ahlrichs, R. Balanced basis sets of split valence, triple zeta valence and quadruple zeta valence quality for H to Rn: Design and assessment of accuracy. *Phys. Chem. Chem. Phys.* **2005**, *7*, 3297–3305.

(74) Weigend, F. Hartree–Fock exchange fitting basis sets for H to Rn. *J. Comput. Chem.* **2008**, *29*, 167–175.

(75) Krzystek, J.; Zvyagin, S. A.; Ozarowski, A.; Trofimenko, S.; Telsler, J. Tunable-frequency high-field electron paramagnetic resonance. *J. Magn. Reson.* **2006**, *178*, 174–183.

(76) Jacques, A.; Clémancey, M.; Blondin, G.; Fourmond, V.; Latour, J.-M.; Sénèque, O. A cyclic peptide-based redox-active model of rubredoxin. *Chem. Commun.* **2013**, *49*, 2915–2917.

(77) Champion, P. M.; Sievers, A. J. Far IR Magnetic-Resonance in FeSiF₆·6H₂O and Fe(SPh)₄²⁻. *J. Chem. Phys.* **1977**, *66*, 1819–1825.

(78) Gülich, P.; Bill, E.; Trautwein, A. X. *Mössbauer Spectroscopy and Transition Metal Chemistry. Fundamentals and Applications*; Springer-Verlag Berlin Heidelberg: 2011.

(79) Zimmerman, R.; Spiering, H.; Ritter, G. Mössbauer spectra of tetrakis-(1,8-naphthyridine) iron(II) perchlorate in external magnetic fields – Evidence of slow relaxation in paramagnetic iron(II). *Chem. Phys.* **1974**, *4*, 133–141.

(80) Stoian, S. A.; Smith, J. M.; Holland, P. L.; Münck, E.; Bominaar, E. L. Mössbauer, Electron Paramagnetic Resonance, and Theoretical Study of a High-Spin, Four-Coordinate Fe(II) Diketiminato Complex. *Inorg. Chem.* **2008**, *47*, 8687–8695.

(81) Bertrand, P.; Gayda, J.-P. A ligand field analysis of the spectroscopic differences between rubredoxin and desulforubredoxin in the reduced state. *Biochim. Biophys. Acta, Protein Struct. Mol. Enzymol.* **1988**, *954*, 347–350.

(82) Bertrand, P.; Gayda, J.-P. A theoretical interpretation of the variations of some physical parameters within the [2Fe-2S] ferredoxin group. *Biochim. Biophys. Acta, Protein Struct. Mol. Enzymol.* **1979**, *579*, 107–121.

(83) Abragam, A.; Bleaney, B. *Electron Paramagnetic Resonance of Transition Ions*; Oxford Univ. Press: New York; 1970

(84) Inspection of Figures S10-S11 reveals that the maximum deviation is less than 5% of the exact values.

(85) Bair, R. A.; Goddard, W. A., III Theoretical studies of the ground and excited states of a model of the active site in oxidized and reduced rubredoxin. *J. Am. Chem. Soc.* **1978**, *100*, 5669–5676.

(86) Our definition of the ω_i angles is included in the caption of Figure S14 of the SI section. A positive ω corresponds to clockwise rotation. For the experimental structure of the reduced Cp-Rd_{red} a negative ω value is observed.

(87) Vrajmasu, V. V.; Münck, E.; Bominaar, E. L. Theoretical Analysis of the Three-Dimensional Structure of Tetrathiolato Iron Complexes. *Inorg. Chem.* **2004**, *43*, 4867–4879.

(88) Vrajmasu, V. V.; Münck, E.; Bominaar, E. L. Theoretical Analysis of the Jahn–Teller Distortions in Tetrathiolato Iron(II) Complexes. *Inorg. Chem.* **2004**, *43*, 4862–4866.

(89) As shown in Figure 6 for $\omega > 22^\circ$ the potential energy of $[\text{Fe}\{(\text{SPH}_2)_2\text{N}\}_2]$ increases exponentially, such that at $\omega = 44^\circ$ the predicted value is 122.71 kcal/mol. Concomitantly, the ΔE_Q variation for $\omega > 22^\circ$ values is much larger than that observed for $0 \leq \omega \leq 22^\circ$, such that at $\omega = 44^\circ$ the predicted theoretical value is $\Delta E_Q = -2.69$ mm/s.

(90) Kramida, A. *Atomic Energy Levels and Spectra Bibliographic Database (version 2.0)*. [Online] Available: <https://physics.nist.gov> [2021, March 4]. National Institute of Standards and Technology: Gaithersburg, MD, 2010; DOI: 10.18434/T40K53. Using the above web site, we obtain the single-electron SOC constants $\zeta_p(\text{S}) = 634.3$ cm^{-1} and $\zeta_p(\text{Se}) = 2917.3$ cm^{-1} .

(91) Coste, S. C.; Vlasisavljević, B.; Freedman, D. E. Magnetic Anisotropy from Main-Group Elements: Halides versus Group 14 Elements. *Inorg. Chem.* **2017**, *56*, 8195–8202.

(92) Karunadasa, H. I.; Arquer, K. D.; Berben, L. A.; Long, J. R. Enhancing the Magnetic Anisotropy of Cyano-Ligated Chromium(II) and Chromium(III) Complexes via Heavy Halide Ligand Effects. *Inorg. Chem.* **2010**, *49*, 4738–4740.

(93) Krzystek, J.; Park, J.-H.; Meisel, M. W.; Hitchman, M. A.; Stratemeier, H.; Brunel, L.-C.; Telser, J. EPR Spectra from “EPR-Silent” Species: High-Frequency and High-Field EPR Spectroscopy of Pseudotetrahedral Complexes of Nickel(II). *Inorg. Chem.* **2002**, *41*, 4478–4487.

(94) Duboc, C.; Phoeung, T.; Zein, S.; Pécaut, J.; Collomb, M.-N.; Neese, F. Origin of the Zero-Field Splitting in Mononuclear Octahedral Dihalide Mn^{II} Complexes: An Investigation by Multi-frequency High-Field Electron Paramagnetic Resonance and Density Functional Theory. *Inorg. Chem.* **2007**, *46*, 4905–4916.

(95) Maganas, D.; Sottini, S.; Kyritsis, P.; Groenen, E. J. J.; Neese, F. Theoretical Analysis of the Spin Hamiltonian Parameters in $\text{Co}^{\text{III}}\text{S}_4$ Complexes, Using Density Functional Theory and Correlated ab initio Methods. *Inorg. Chem.* **2011**, *50*, 8741–8754.